

# Constraining the rheology of the Earth

(651-4008-00 G)

# Schedule

- Constraints on the rheology from
  1. the laboratory,
  2. geology,
  3. geophysics and
  4. numerical modelling

# ***Laboratory constraints***

# Viscous creep law

- Experimental data
- The viscosity of rocks is strongly dependent on  
pressure, temperature, stress (strain-rate),  
grain size, water content, melt and mineralogy, ...

## Arrhenius flow law

$$\dot{\epsilon} = A \tau^n d^{-p} C_{OH}^s \exp(-\alpha\phi) \exp\left[\frac{-(E + PV)}{RT}\right]$$

## Effective viscosity

$$\eta_{\text{effective}} = \frac{\tau}{\dot{\epsilon}}$$

# Upper mantle

$$\dot{\epsilon} = A \left( \frac{\tau}{\mu} \right)^n \left( \frac{b}{d} \right)^m \exp \left[ -\frac{(E^* + pV^*)}{RT} \right]$$

**Table 5.3. Parameter Values for Diffusion Creep and Dislocation Creep in a Dry Upper Mantle<sup>a</sup>**

Quantity	Diffusion Creep	Dislocation Creep
Pre-exponential factor $A$ ( $\text{s}^{-1}$ )	$8.7 \times 10^{15}$	$3.5 \times 10^{22}$
Stress exponent $n$	1	3.5
Grain size exponent $m$	3	0
Activation energy $E^*$ ( $\text{kJ mol}^{-1}$ )	300	540
Activation volume $V^*$ ( $\text{m}^3 \text{mol}^{-1}$ )	$6 \times 10^{-6}$	$2 \times 10^{-5}$

<sup>a</sup> After Karato and Wu (1993). Other relevant parameter values are  $\mu_{\text{shear modulus}} = 80 \text{ GPa}$ ,  $b = 0.55 \text{ nm}$ , and  $R = 8.3144 \text{ J K}^{-1} \text{ mol}^{-1}$ .

# Fracture style as a function of confining pressure

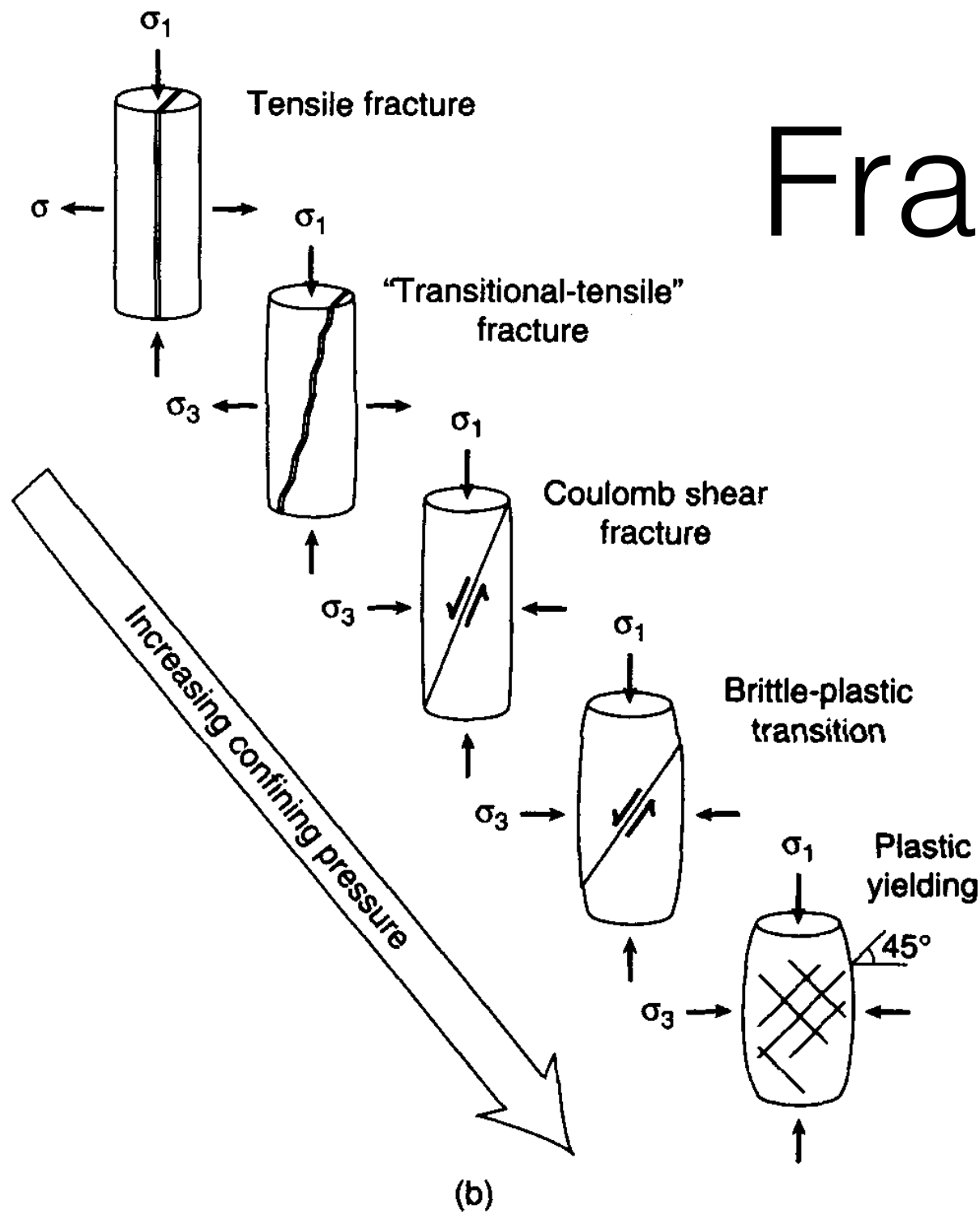
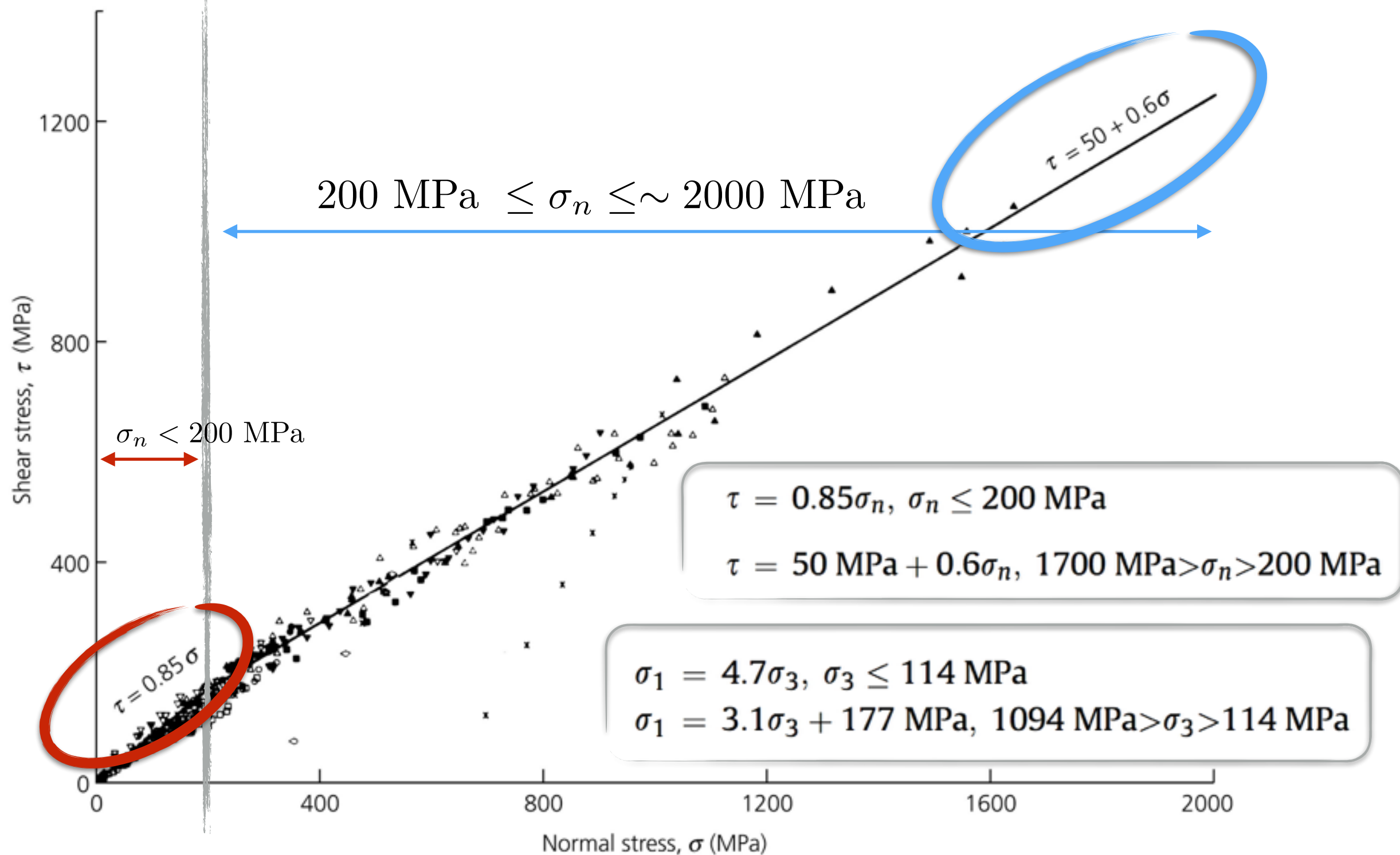


**Figure 6.25** (a) A representative composite failure envelope on a Mohr diagram. The different parts of the envelope are labeled, and are discussed in the text. (b) Sketches of the fracture geometry that forms during failure. Note that the geometry depends on the part of the failure envelope that represents failure conditions, because the slope of the envelope is not constant.

# Byerlee's law

[http://geophysics.eas.gatech.edu/people/anewman/classes/Geodynamics/misc/5\\_7\\_10.jpg](http://geophysics.eas.gatech.edu/people/anewman/classes/Geodynamics/misc/5_7_10.jpg)

**Figure 5.7-10: Relation between shear stress and normal stress for frictional sliding.**



# Strength of the mantle-lithosphere

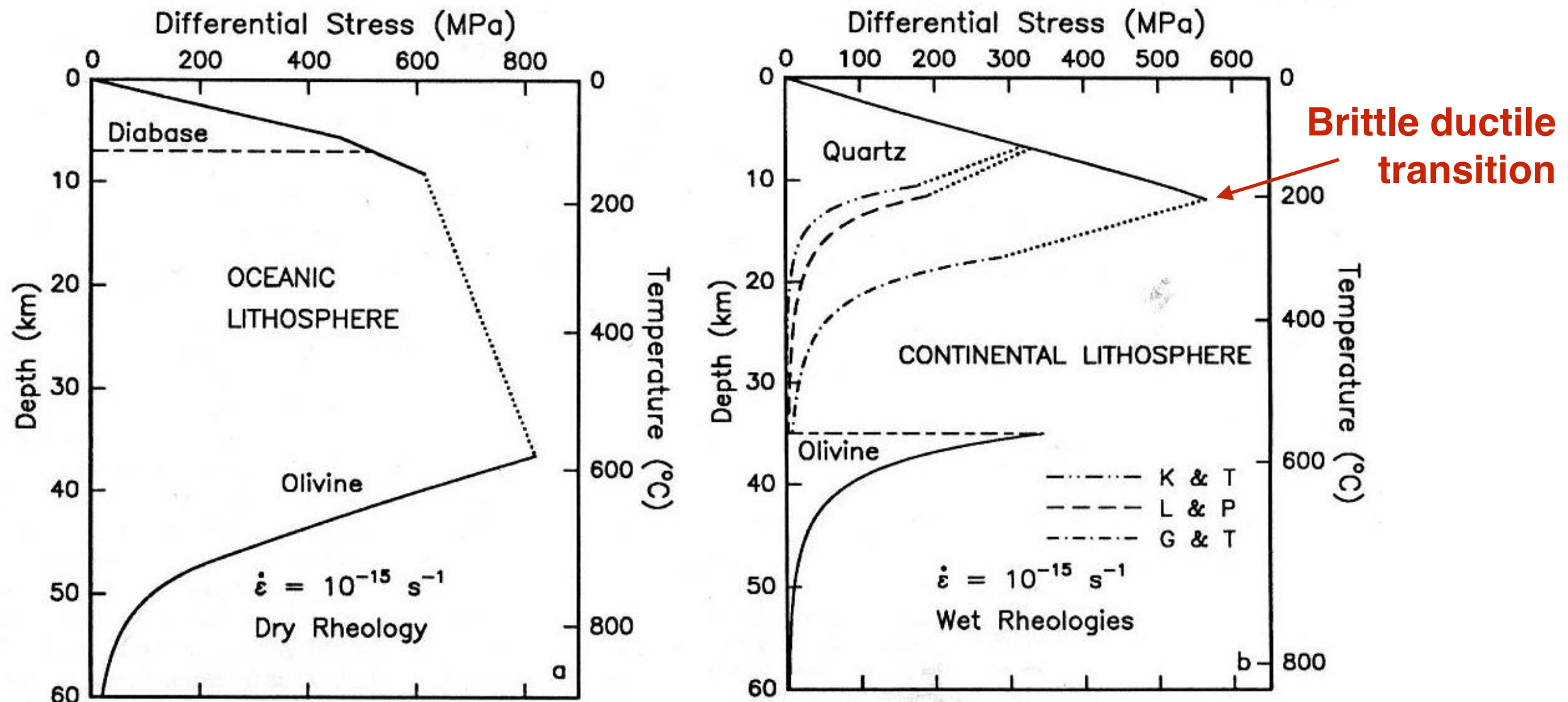


**Figure 9.** Strength envelopes for oceanic and continental lithosphere. (a) For the oceanic lithosphere, a geotherm for 60-m.y.-old lithosphere was used [e.g., *Turcotte and Schubert, 1982* pp. 163-167]. A rheology for dry olivine [*Chopra and Paterson, 1984*] was used because water strongly partitions into the melt during partial melting. (b) For the continental lithosphere, a geotherm for a surface heat flow of  $60 \text{ mW m}^{-1}$  was employed [*Chapman, 1986*]. The rheologies for wet quartzite are those used in Figure 5; the olivine rheology is for wet Anita Bay dunite from *Chopra and Paterson [1984]*. Wet rheologies were used, consistent with high fluid pressures in fault zones. Plastic flow strength was corrected for water fugacity using a water fugacity exponent of unity and assuming lithostatic pore pressure. The BDT and BPT, determined as described in the text, have been connected by a dotted line.

# Compression versus extension

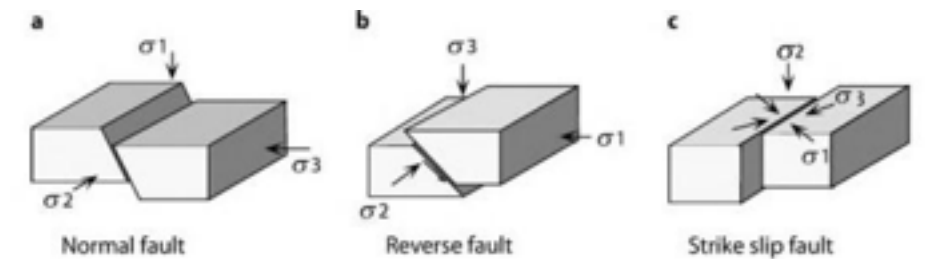
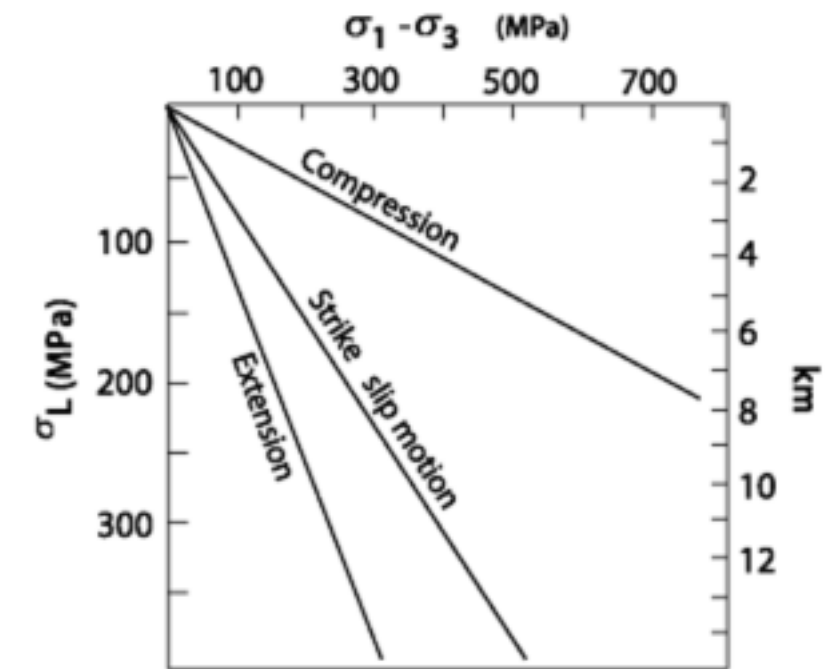
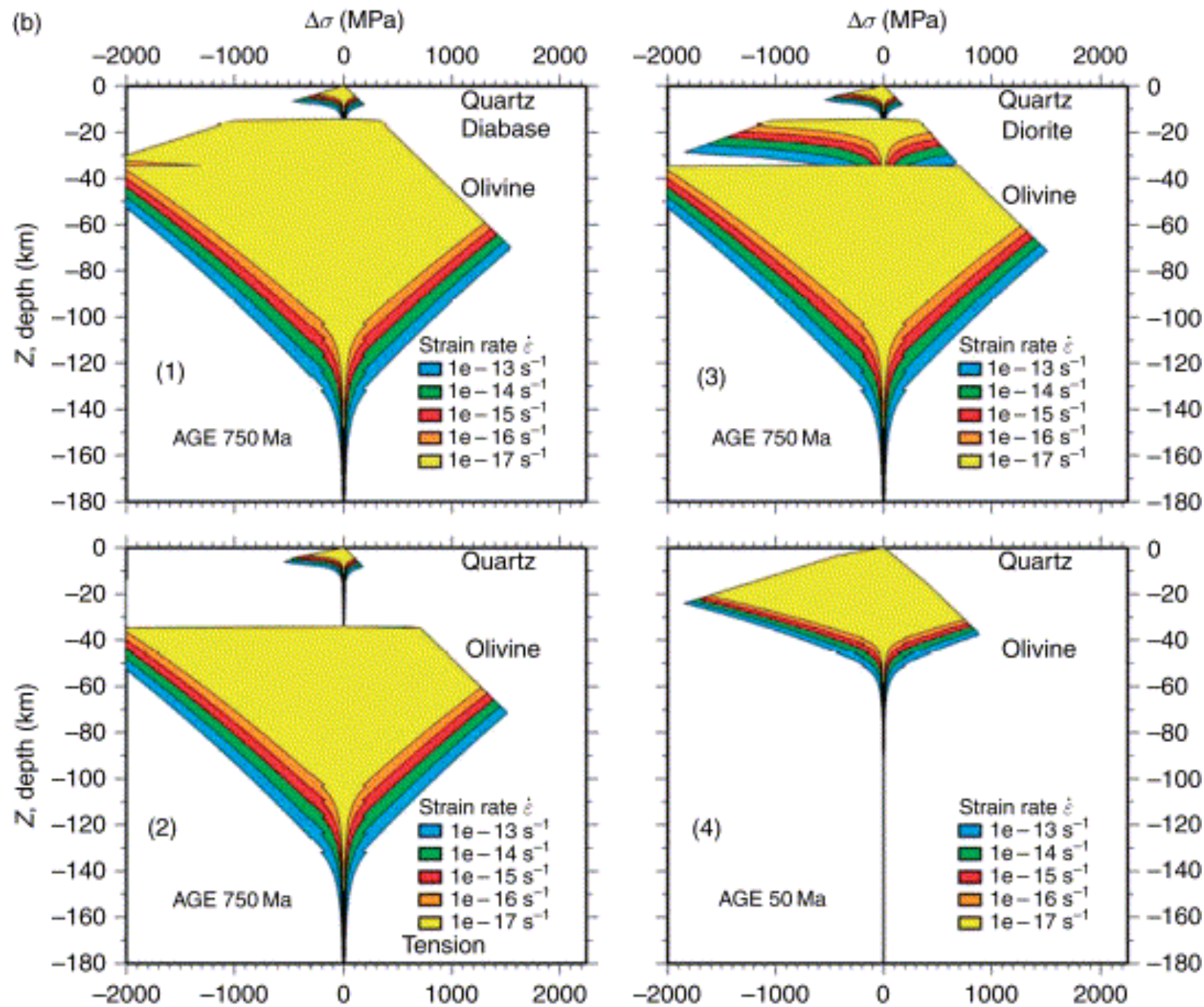
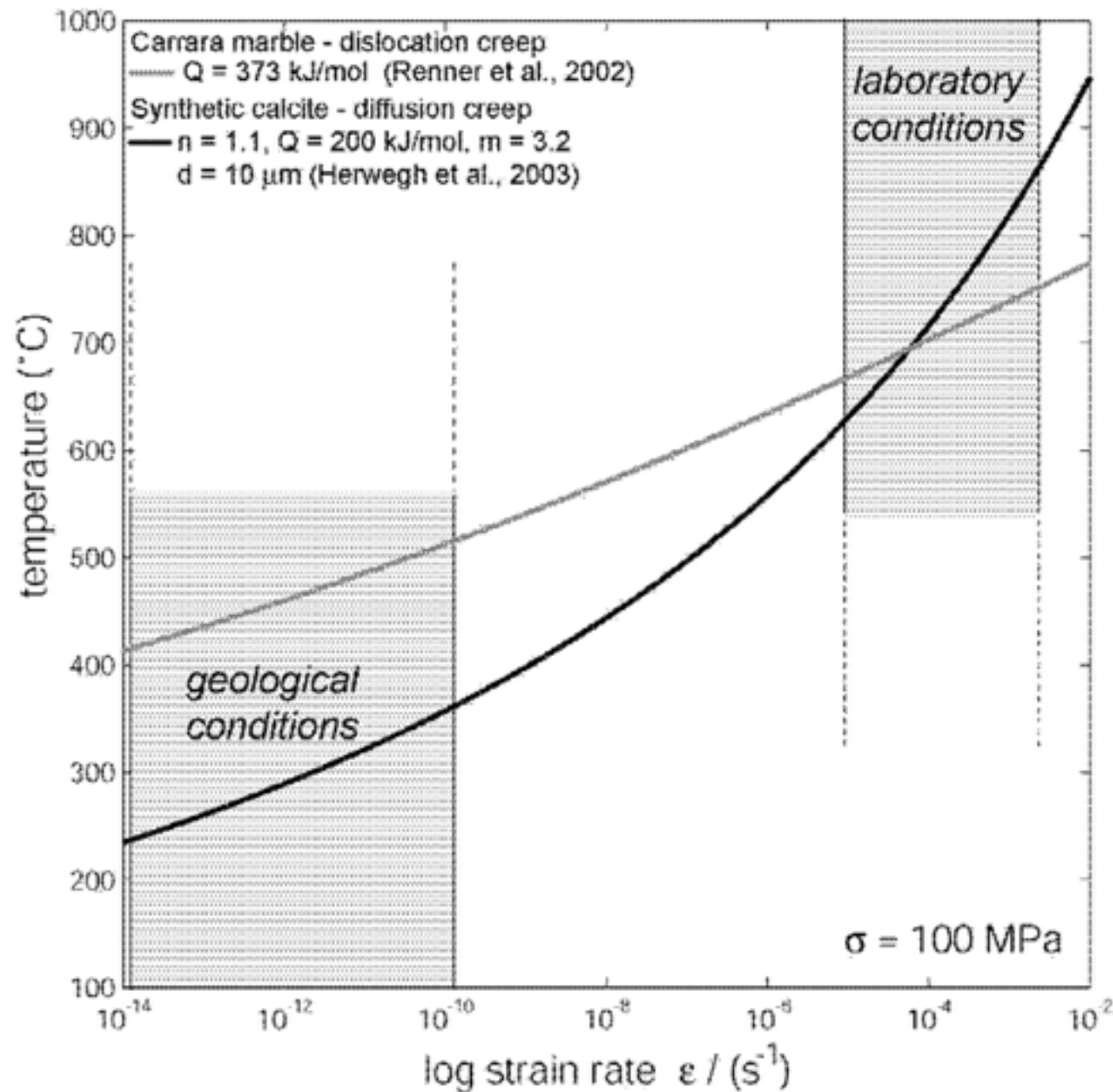


Figure 5.8. Geometry of a brittle fault during: a extension, b compression and c strike slip motion

Difference come from the dependence of Byerlee's law on the normal stress  
 Compression results in large normal stress (tectonic loading)

# Limitations of the lab



- Extrapolation over many orders of magnitude in strain-rate
- Relatively low strain experiments
- Generally mono-mineralic
- Small samples in lab. - are large scale heterogeneities important?
- Effects of water, melt not included or difficult to control

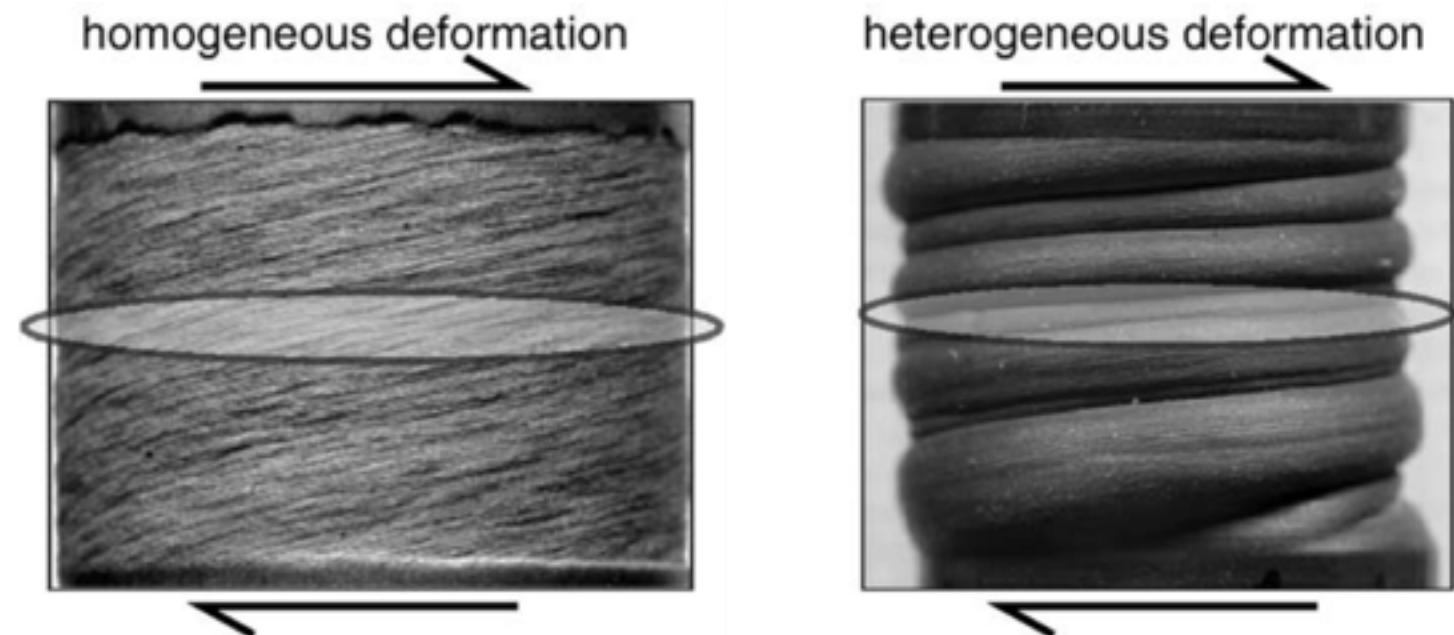
# Two-phase experiments

(Barnhoorn et al, EPSL, 2005)

Calcite  
 $\text{CaCO}_3$

Anhydrite  
 $\text{CaSO}_4$

- Calcite (or anhydrite) deformed in isolation result in homogenous deformation up to large strains
- Mixtures of calcite and anhydrite result in heterogeneous deformation and shear localisation



**anhydrite**  
(white/light grey)  
**calcite**  
(dark gray)

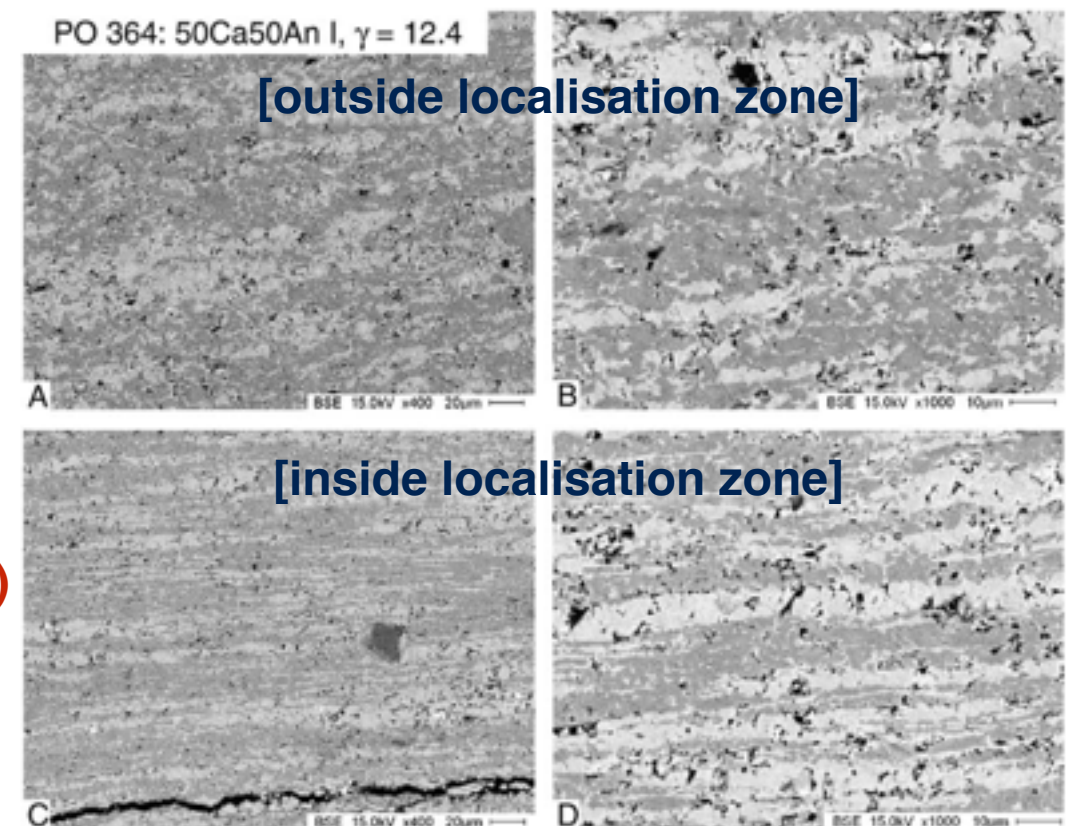


Fig. 5. BSE images of sample PO364 (50Ca50An I),  $\gamma_{\text{bulk}} \sim 12$  at different magnifications (greyscale contrasts same as in Fig. 4). (A+B) Outside localised zone. (C+D) Inside localised zone.

# Two-phase experiments

- *Low strain, homogeneous deformation*
- *Strain localisation occurs only at high strain*
- Heterogeneous material induces local strength variations initiating strain localisation
- Deformation mechanism in anhydrite changes from dislocation creep to diffusion creep with strain localisation

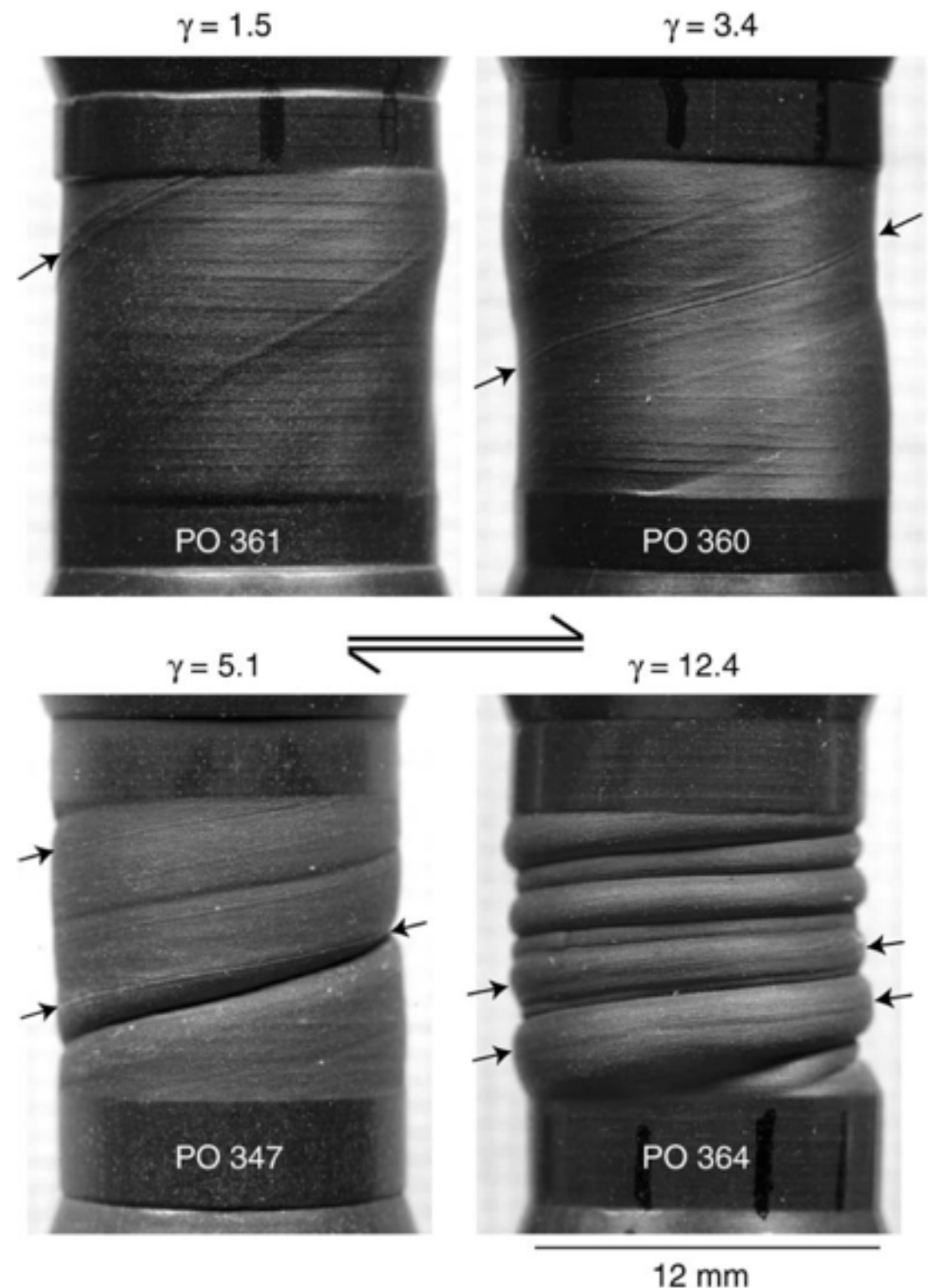
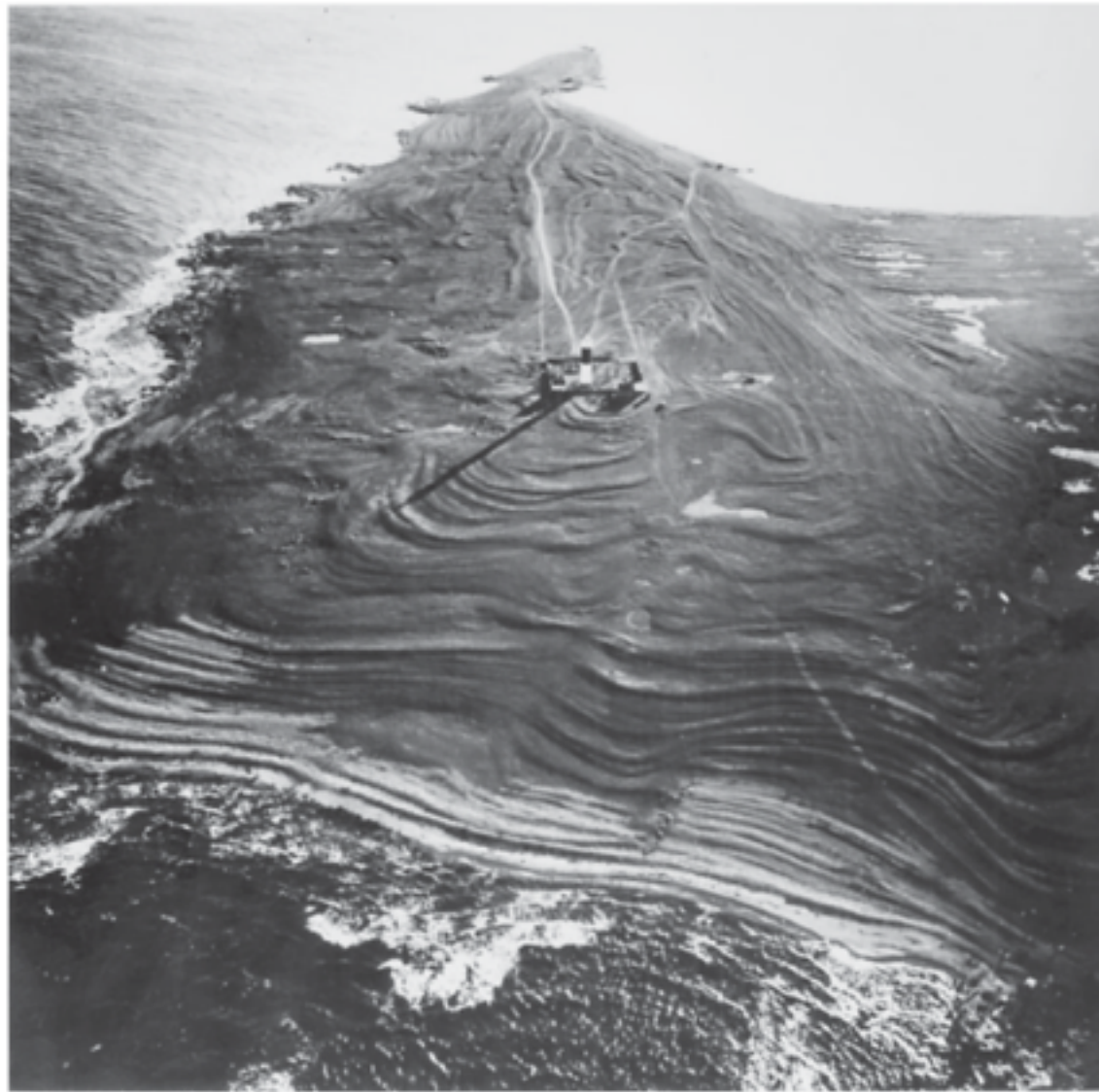


Fig. 2. Progressive change in shape of heterogeneously deformed 50Ca50An I samples deformed to various amounts of shear strain. The samples, flanked with alumina pistons of the same diameter at the top and bottom, are still in their iron jackets. Oblique lineaments/grooves (indicated with arrows) are indentations or markers on the iron jacket and are used to analyse the strain distribution.

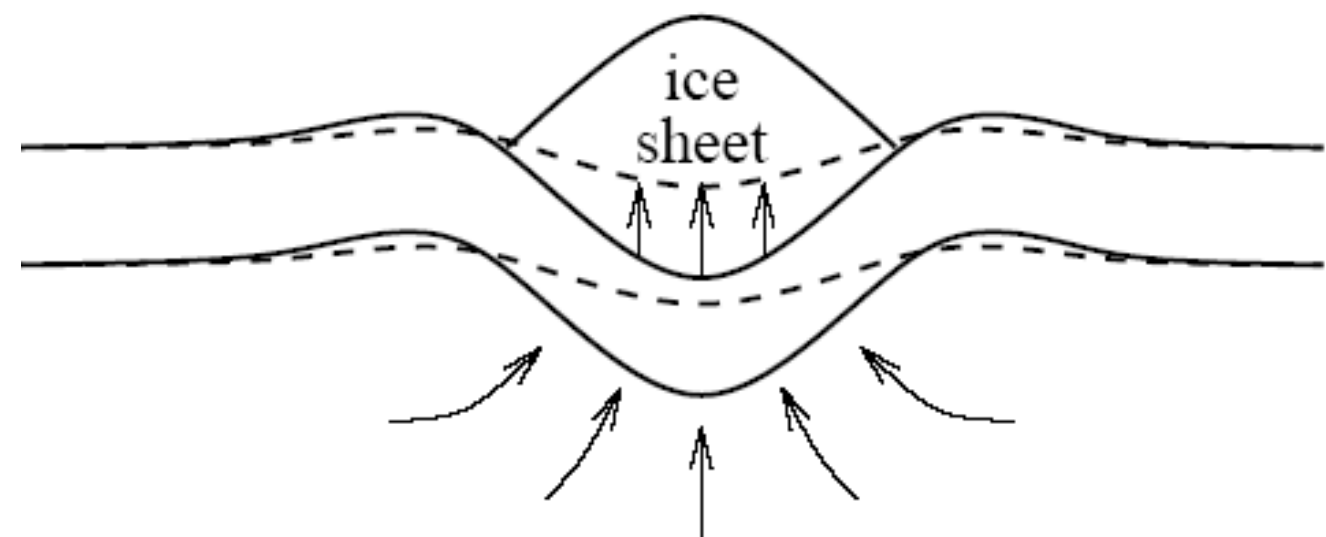
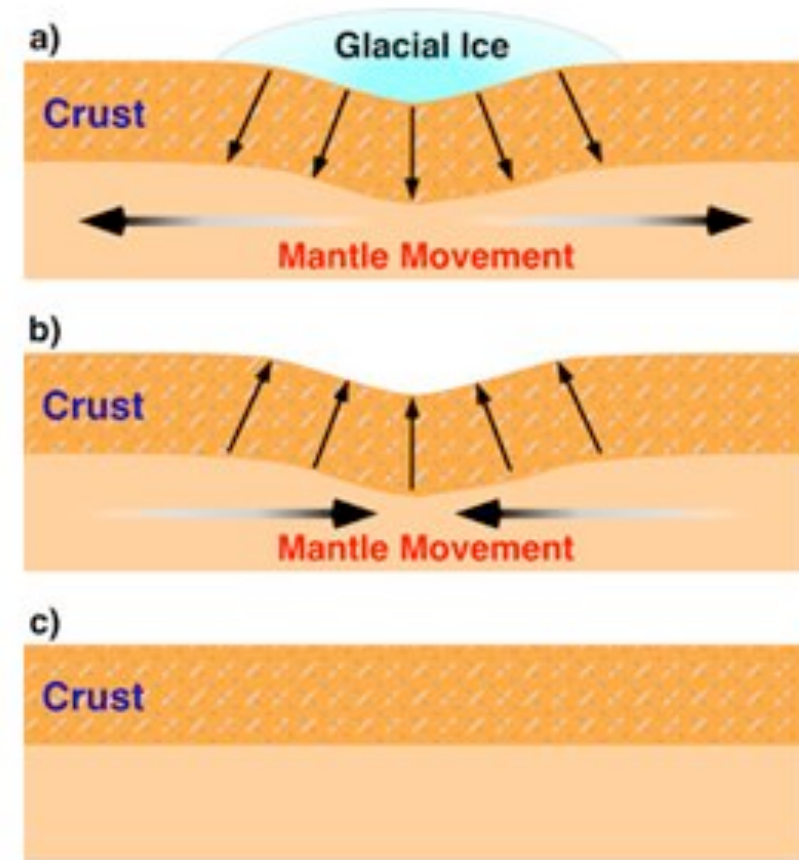
# ***Observational constraints***

# Postglacial rebound



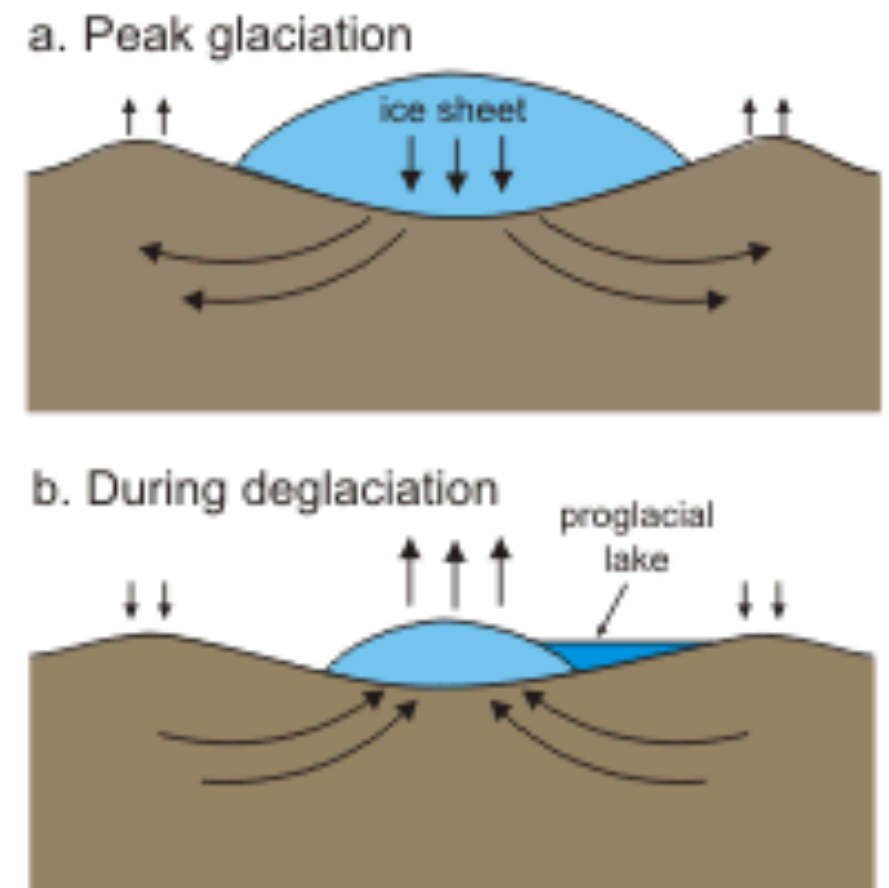
**Figure 6.15** Elevated beach terraces on Östergransholm, Eastern Gotland, Sweden. The contemporary uplift rate is about  $2 \text{ mm yr}^{-1}$ . (Photographer and copyright holder, Arne Philip, Visby, Sweden; courtesy IGCP Project Ecostratigraphy.)

(Turcotte & Schubert, 2014)



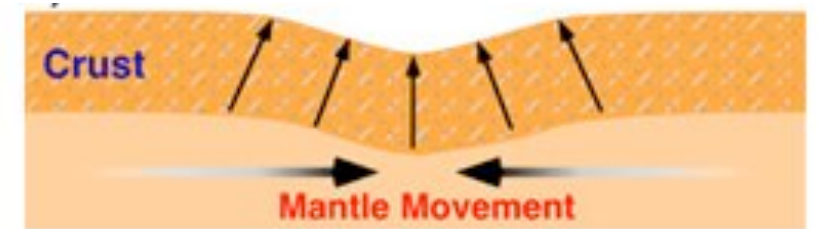
# Postglacial rebound

- The rate of rebound is sensitive to the absolute viscosity
- Rate of rebound depends on
  - ice-load size/shape, sea-level measurements and unloading history
  - lateral variations in elastic plate properties



# Postglacial rebound

- Assume periodic displacement,  $w_m$
- Semi-infinite viscous half space
- Displacement leads to horizontal pressure gradient



$$w_m = w_m^0 \cos(2\pi x / \lambda)$$

$$w = w_m e^{-t/\tau_r},$$

$$\tau_r = \frac{4\pi\mu}{\rho g \lambda}$$

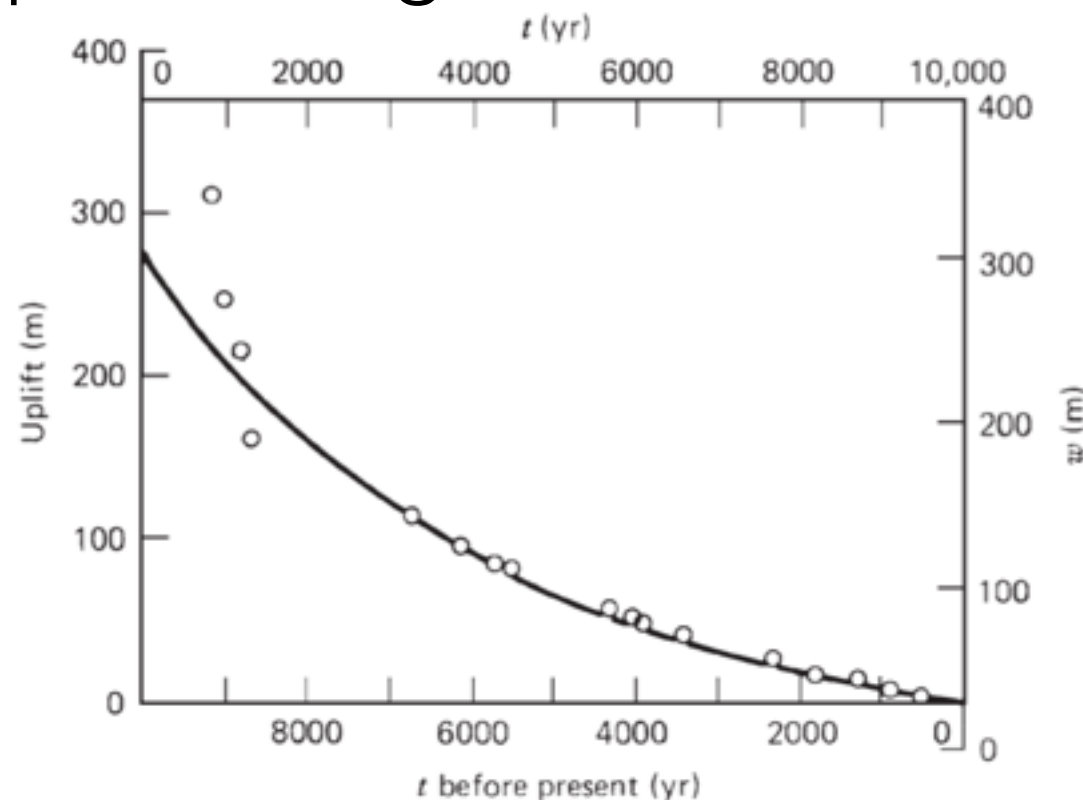


**Figure 6.16** Uplift of the mouth of the Angerman River, Sweden, as a function of time before the present compared with the exponential relaxation model, Equation (6.104), for  $w_{m0} = 300$  m less 30 m of uplift yet to occur,  $\tau_r = 4400$  years, and an initiation of the uplift 10,000 years ago.

**Table 6.2** Distribution of Viscosity in the Mantle from Postglacial Rebound Studies

Region	Depth (km)	Dynamic Viscosity (Pa s)
Lithosphere	0–100	Elastic
Asthenosphere	100–175	$4 \times 10^{19}$
	175–2848	$10^{21}$

# Postglacial rebound

- Haskell (1935) estimated the average viscosity for the mantle to be  $1e21$  Pa s
- Results from more recent inversions constrained by PGR

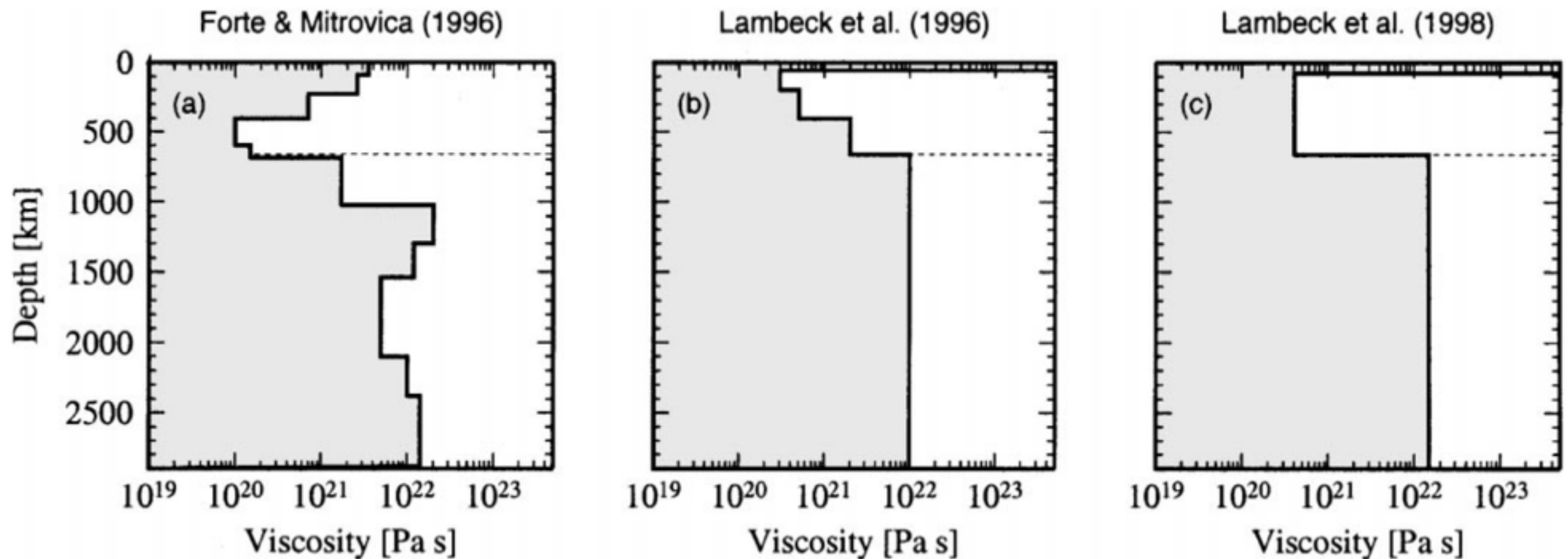
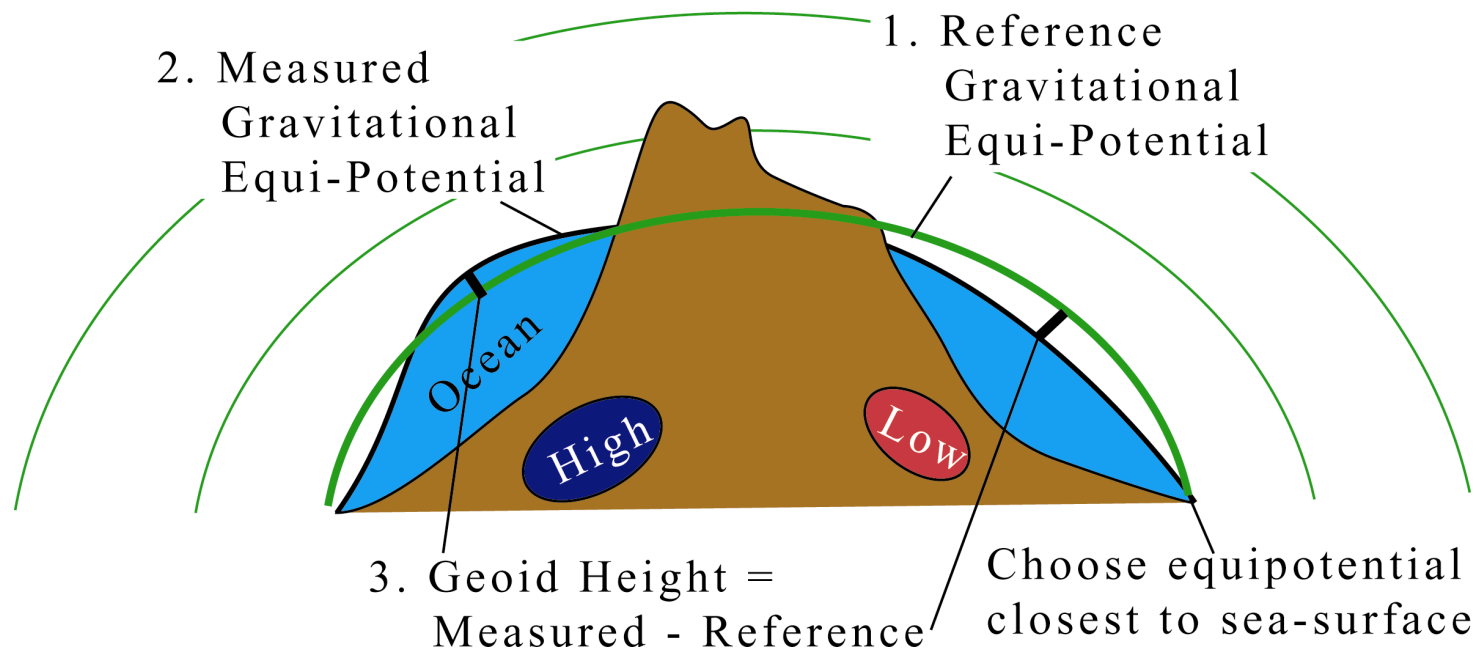


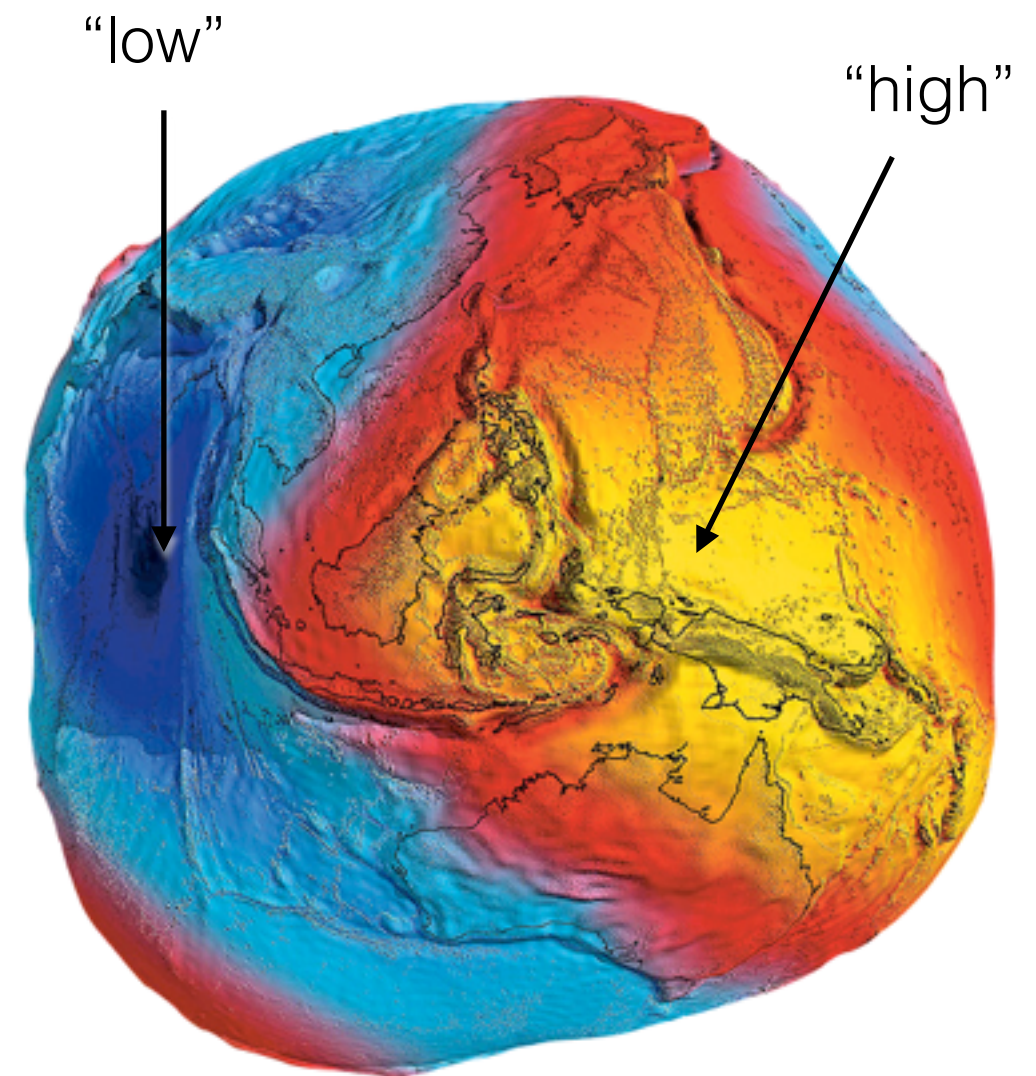
Fig. 2. Scaled viscosity profiles from predictions of postglacial rebound signatures.

# Geoid



(from Magali Billen)

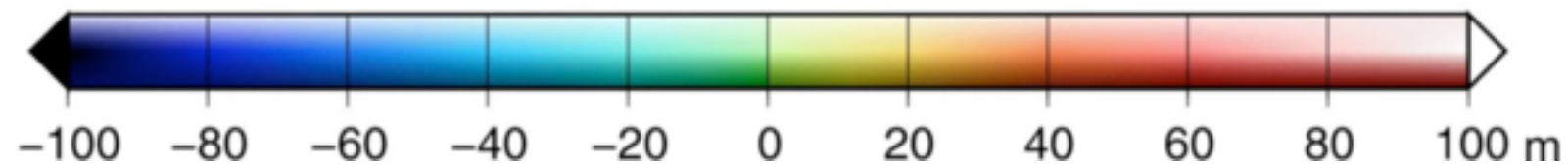
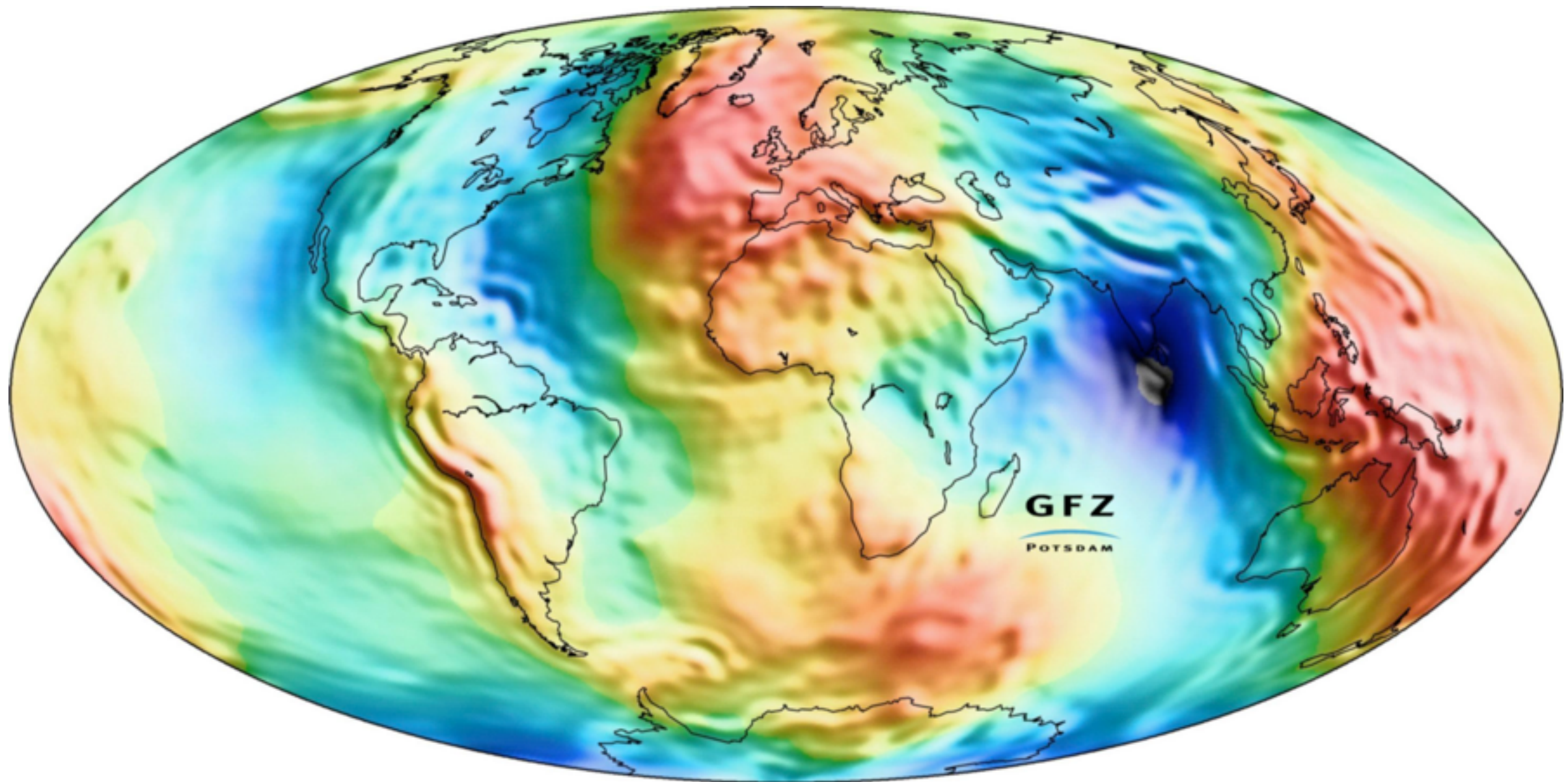
- Geoid is the surface of an ideal global ocean in the absence of tides - only shaped by gravity
- Sensitive to deep mantle (low wavelength) structures



Geoid as measured by GOCE (Gravity field and steady-state Ocean Circulation Explorer) ESA

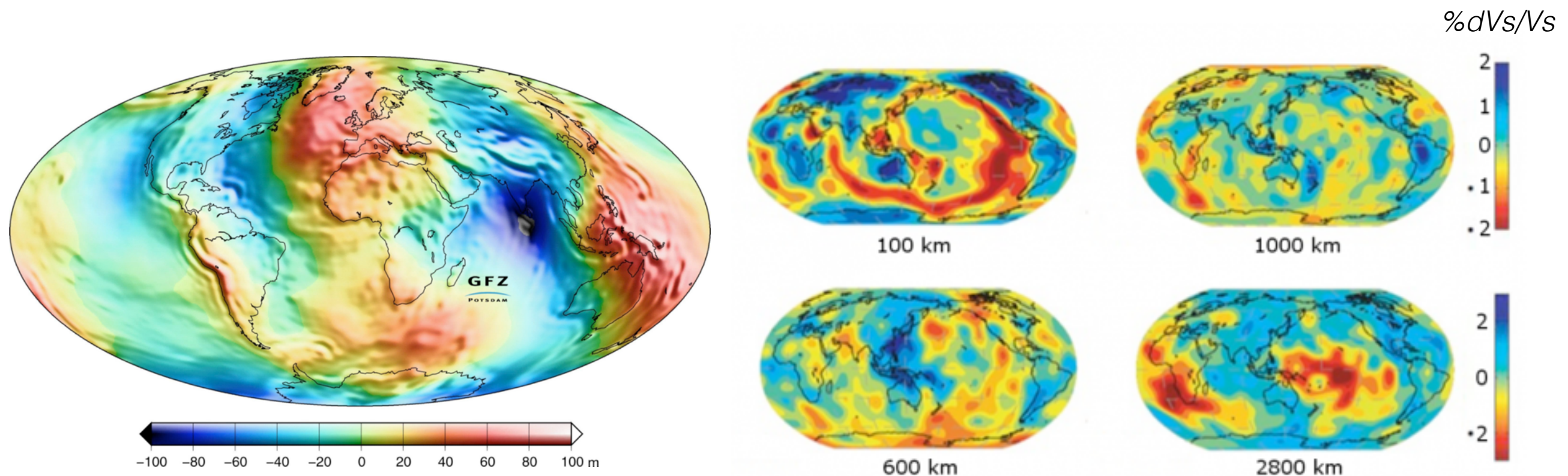
# Geoid

- Range is on the order of +/- 120 meters



# Geoid

- Observations from seismic studies
  - Long wavelength geoid *LOWs* correlate with seismically *FAST* regions, i.e. cold (dense) regions
  - Long wavelength geoid *HIGHS* correlate with seismically *SLOW* regions, i.e. hot buoyant regions



# Geoid

- A. Static (elastic) model produces only positive geoid (mass excess)
- B. Deformed surface results in mass deficit
- C. Viscosity contrast between upper / lower mantle required to fit geoid data

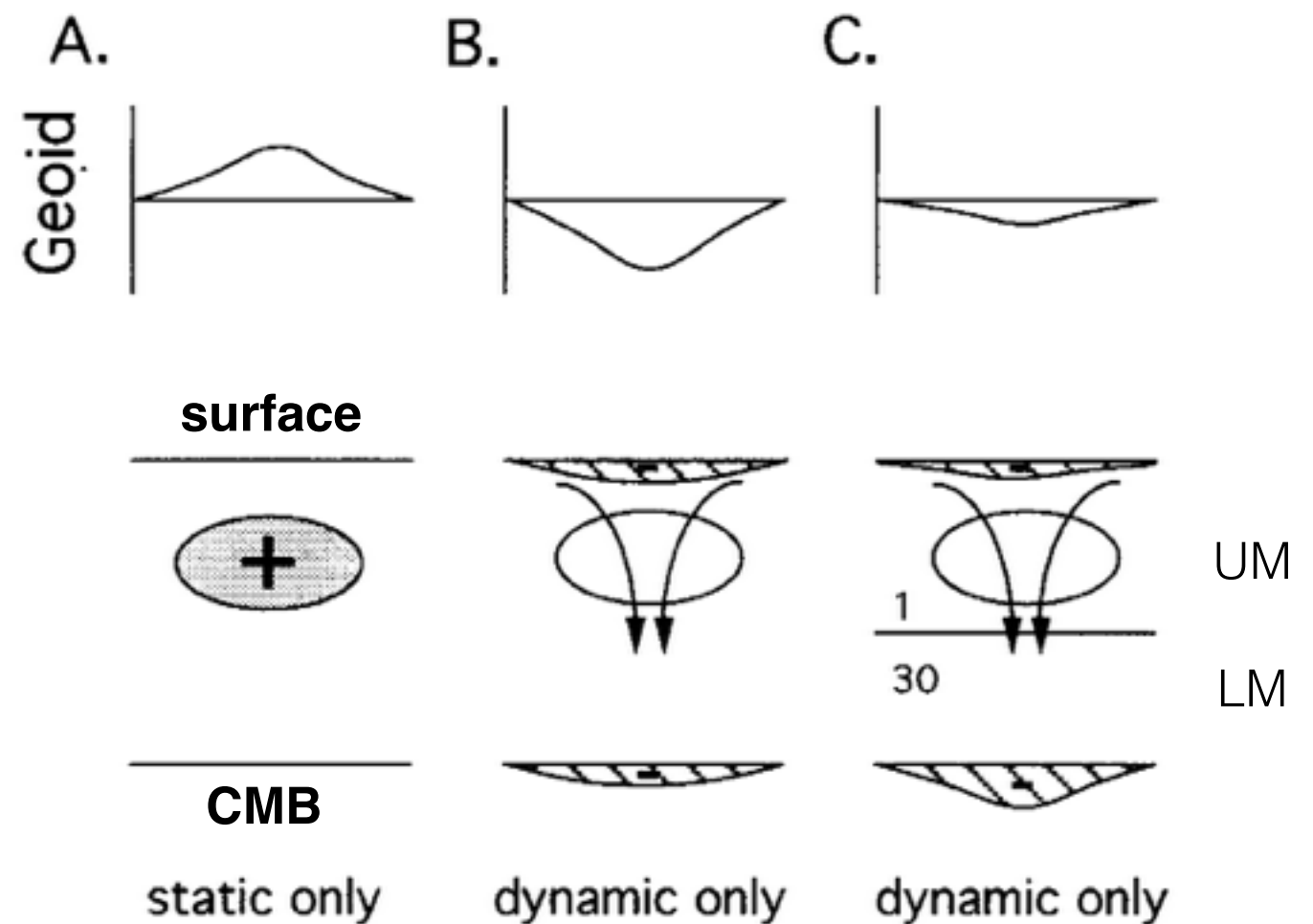
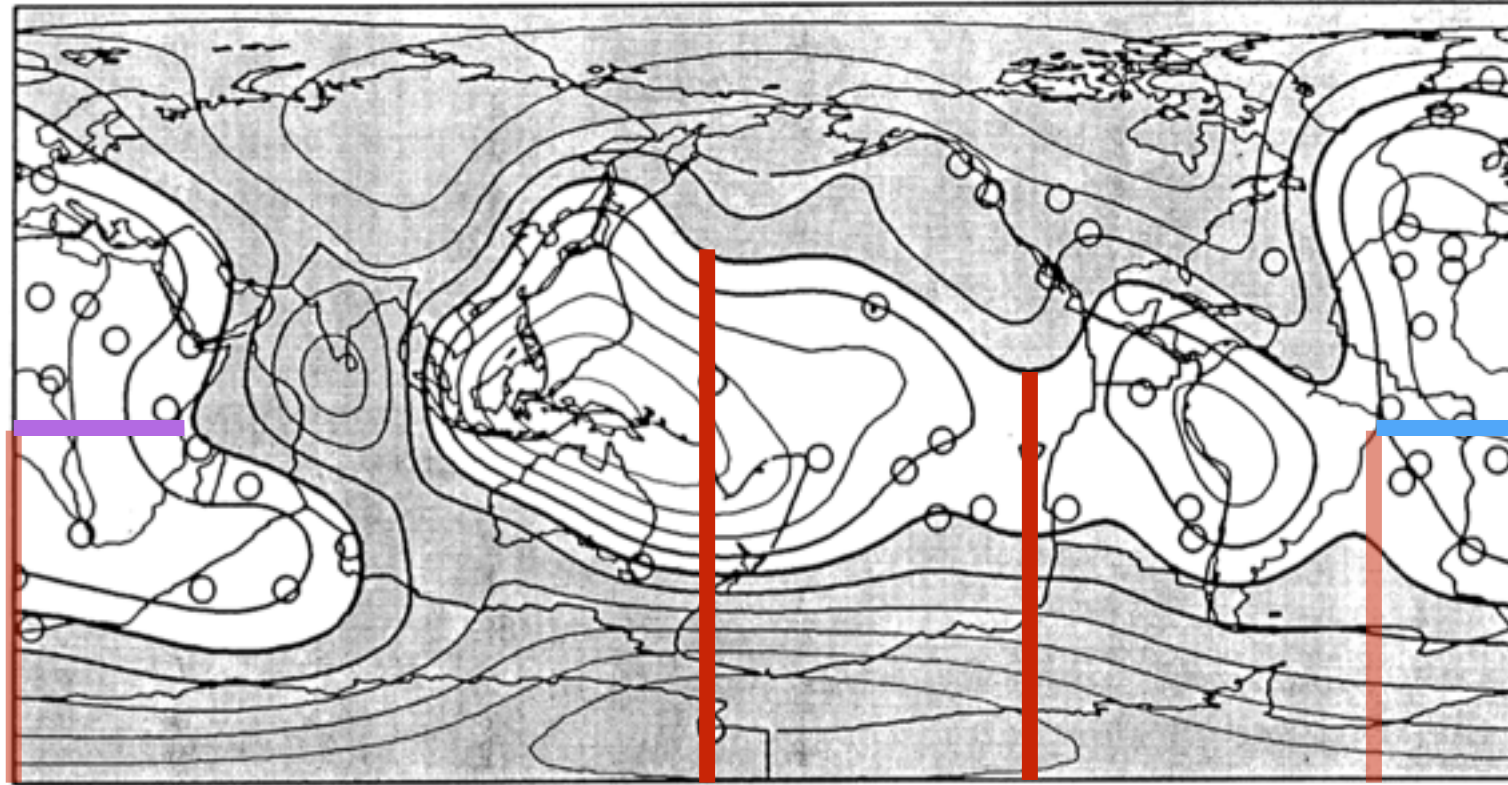


Fig. 2. (a) The geoid anomaly over a positive mass anomaly (stippled) in a static earth. (b) The dynamic flow driven by the mass anomaly causes negative mass anomalies (stippled regions) at the upper and lower boundaries, hence negative geoid anomalies. The sum of (a) and (b) is a negative anomaly in a uniform viscosity medium. (c) With an increased viscosity in the lower layer, the dynamic topography of the surface is reduced and the sum of (a) plus (c) could be positive.

(King, Models of mantle viscosity, *Mineral physics and crystallography*, 1995)

Measured



Computed  
- Using 30x  
higher  
viscosity at  
660 km

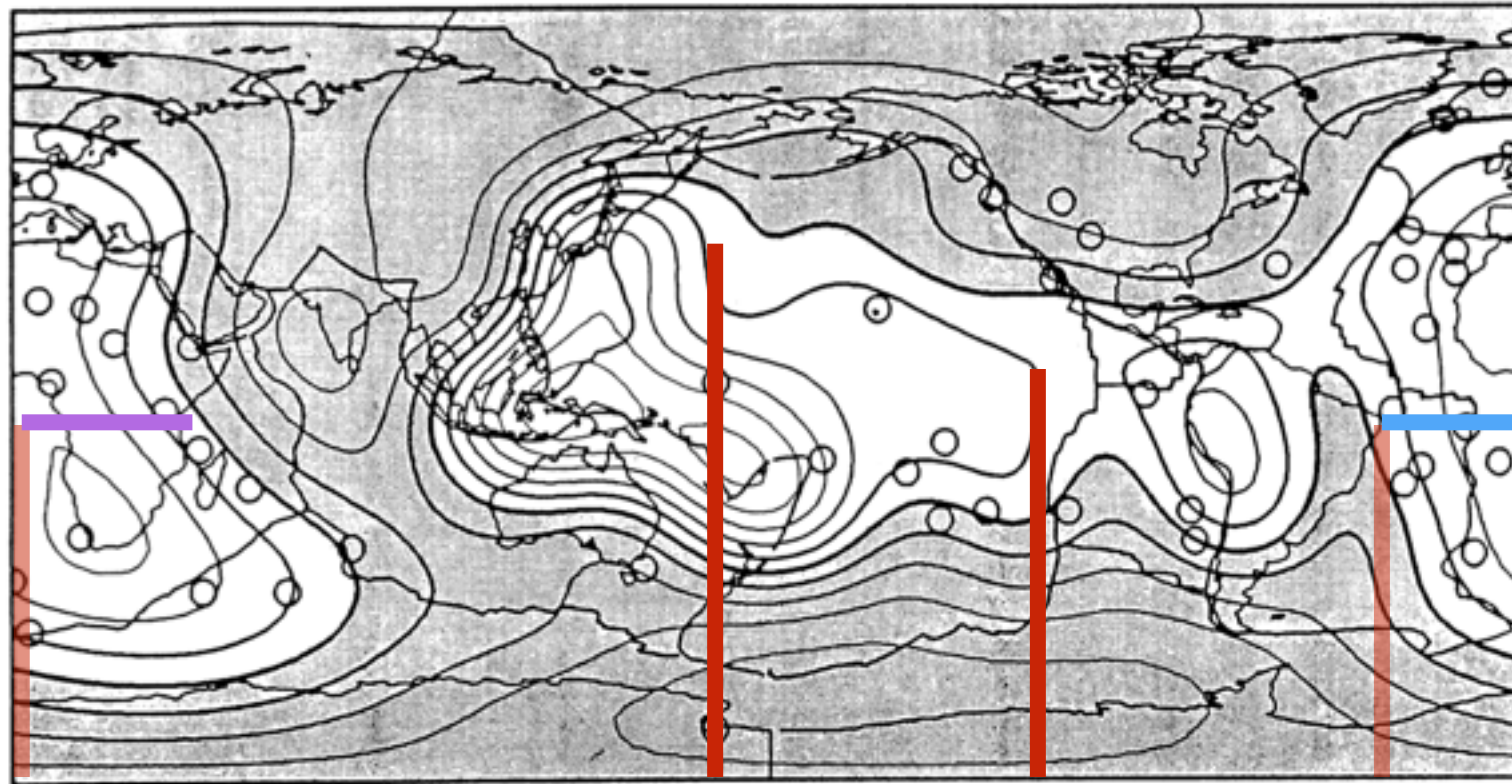
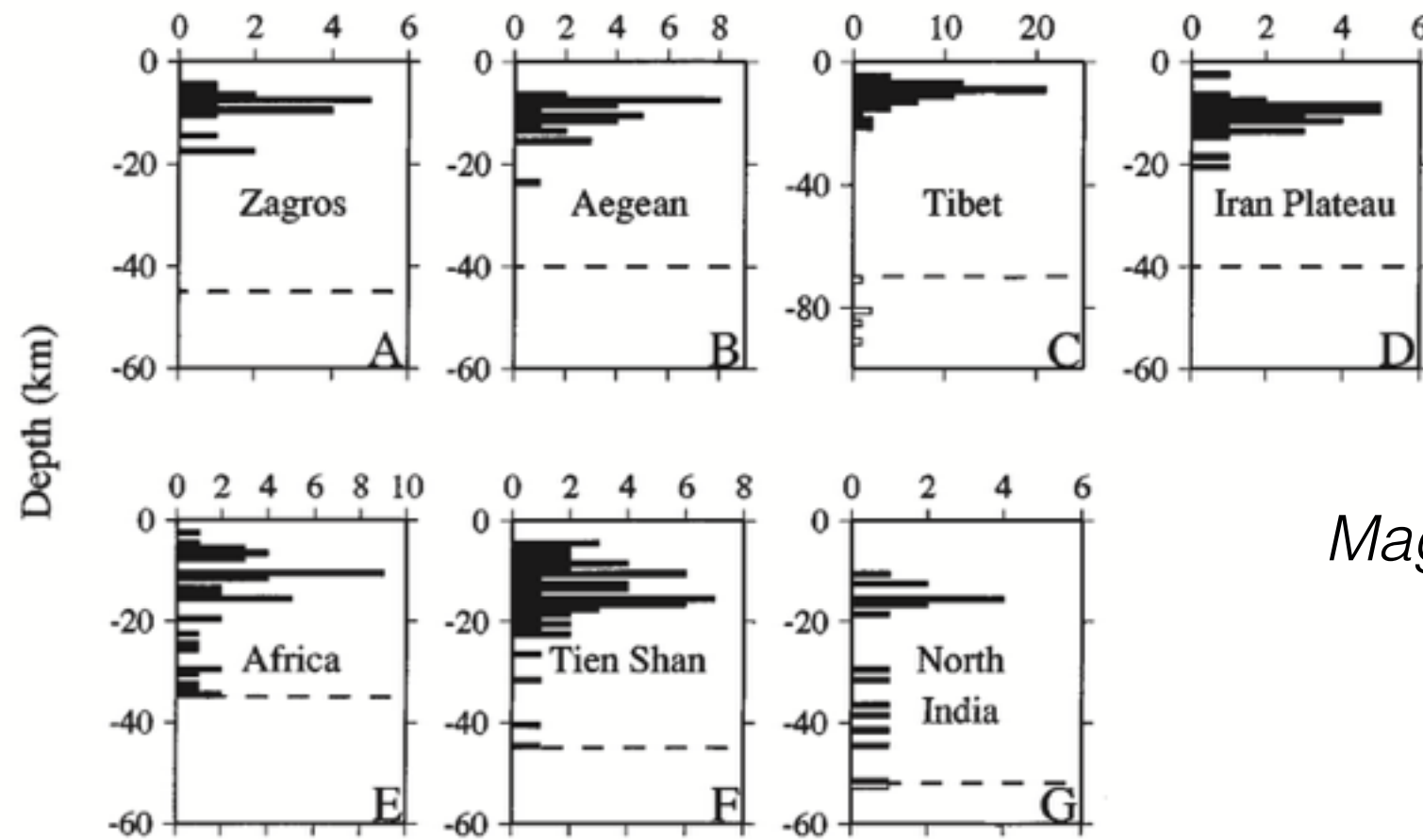


Figure 5.11. Comparison of nonhydrostatic geoid (top) and geoid computed from lower mantle seismic heterogeneity and dynamic topography in a two-layer mantle model with a factor 30 increase in viscosity at 660 km depth (bottom). Shaded regions are negative; unshaded regions are positive relative to the hydrostatic geoid. From Hager and Richards (1989).

# Seismicity



*Maggi et al, (2000)*

**Figure 1. Histograms of earthquake focal depths determined by modeling of long-period teleseismic P (primary) and SH (secondary horizontal) seismograms (solid bars). White bar in North India (G) is depth determined from short period depth phases in Shillong Plateau by Chen and Molnar (1990). White bars in Tibet (C) are subcrustal earthquakes, but not necessarily in mantle of continental origin. Approximate Moho depths are indicated by dashed lines. Focal depth and Moho data are from various sources, including Nelson et al. (1987), Molnar and Lyon-Caen (1989), Foster and Jackson (1998), Mangino et al. (1999), and Maggi et al. (2000). Focal depths based on arrival times recorded at local seismic networks have also found seismicity throughout crust in several parts of North America (e.g., Wong and Chapman, 1990).**

- Most earthquakes occur within the upper crust, few beneath the Moho (dashed line)

# Seismicity

*Jackson (2002)*

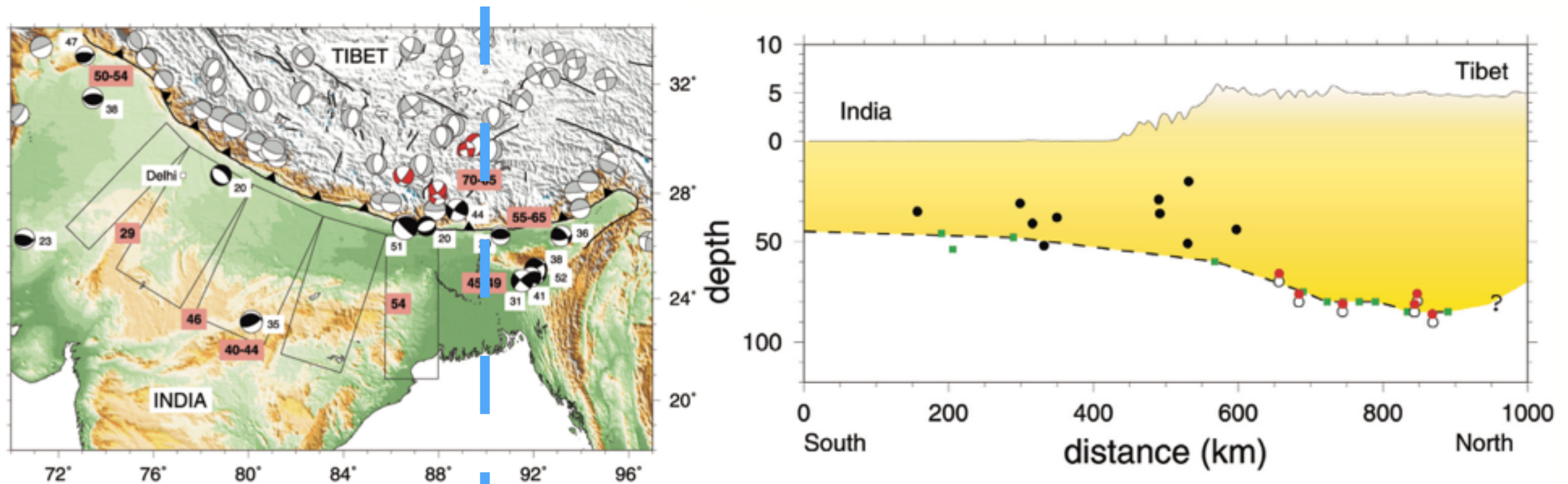
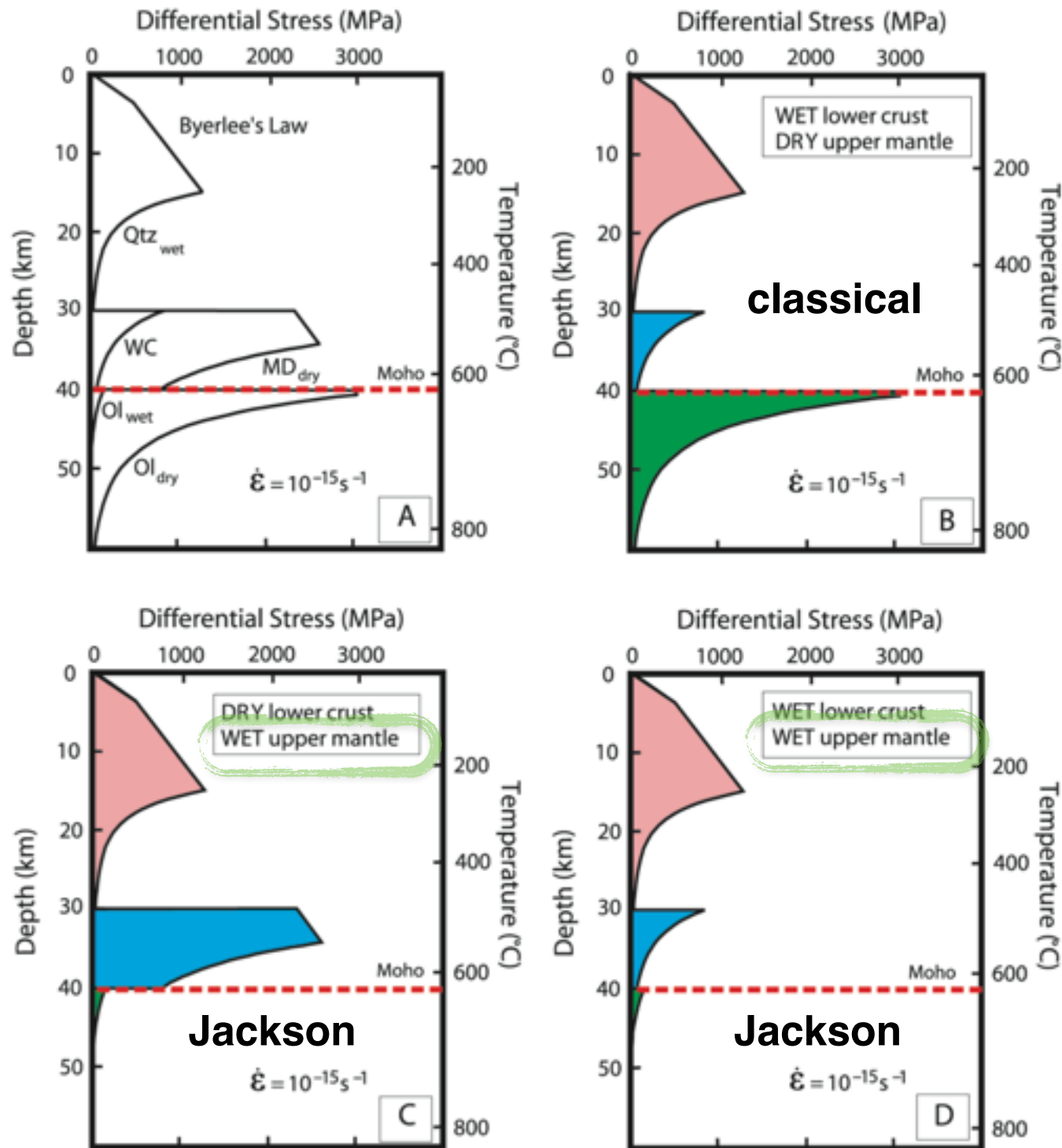


**Figure 2.** A cross section through Figure 1 along 90°E (note the different vertical exaggeration above and below sea level), with earthquakes and Moho depths projected onto the profile from up to 400 km on either side (in addition, the event at 35 km depth at 24°N 80°E has been included). Black and red symbols correspond to the same colored earthquakes in Figure 1. The red earthquakes have had their depths reduced by 4 km from their published depths (open circles) to allow for the overlying crustal velocities (see text). Green squares are Moho depth determinations, joined by a dotted line separating crust (yellow) from mantle.

# Seismicity



- “Classical” model - strength lies within the crust AND mantle
- Lack of earthquakes below 40 km implies low strength material
- Low strength → “weak”
- Strength lies only within the crust

**Figure 5.** Strength envelopes of differential stress (essentially rock strength) versus depth for various continental conditions, to illustrate the potential effects of water (adapted from Mackwell et al., 1998). The Moho is at 40 km and the temperature variation with depth corresponds to a surface heat flow of  $60 \text{ mWm}^{-2}$ . In all cases, the upper crust is represented by wet quartz (Qtz) and frictional strength by Byerlee's law. **A.** A summary of experimental results, in which the lower crust is represented by dry diabase (MD) or undried granulite (WC), and the mantle by dry or wet olivine (Ol). **B.** Wet lower crust and dry upper mantle, showing the popular conception of the continental lithosphere for the past 20 years, involving a weak lower crust and strong upper mantle. **C.** Dry lower crust and wet upper mantle, showing a strong lower crust over a mantle that has no strength, which may represent conditions under some continental shields, such as north India. **D.** Wet lower crust and wet upper mantle, neither of which have significant strength. In this case, nearly all strength resides in the seismogenic upper crust, which may represent conditions in most continental areas.

*Jackson (2002)*

# ***Constraints from numerics***

# Plate motions: Radial structure

- Plate motions result from a balance of buoyancy forces (driving motion) and viscous stresses (resisting motion)
- Plate motion is directly measured from GPS
- Buoyancy anomalies at depth inferred from seismic tomography
- Joint inversion using
  - (a) forward model given by incompressible Stokes with Boussinesq approximation
  - (b) geoid and plate motion data define objective function (misfit)
- Linear super-position of two flow solutions: (i) no buoyancy variations - plate motion imposed as boundary condition; (ii) tomography - plate motion assumed to zero
- Look for RADIAL viscosity profiles which yield zero net torque on each lithospheric plate

# Comparisons

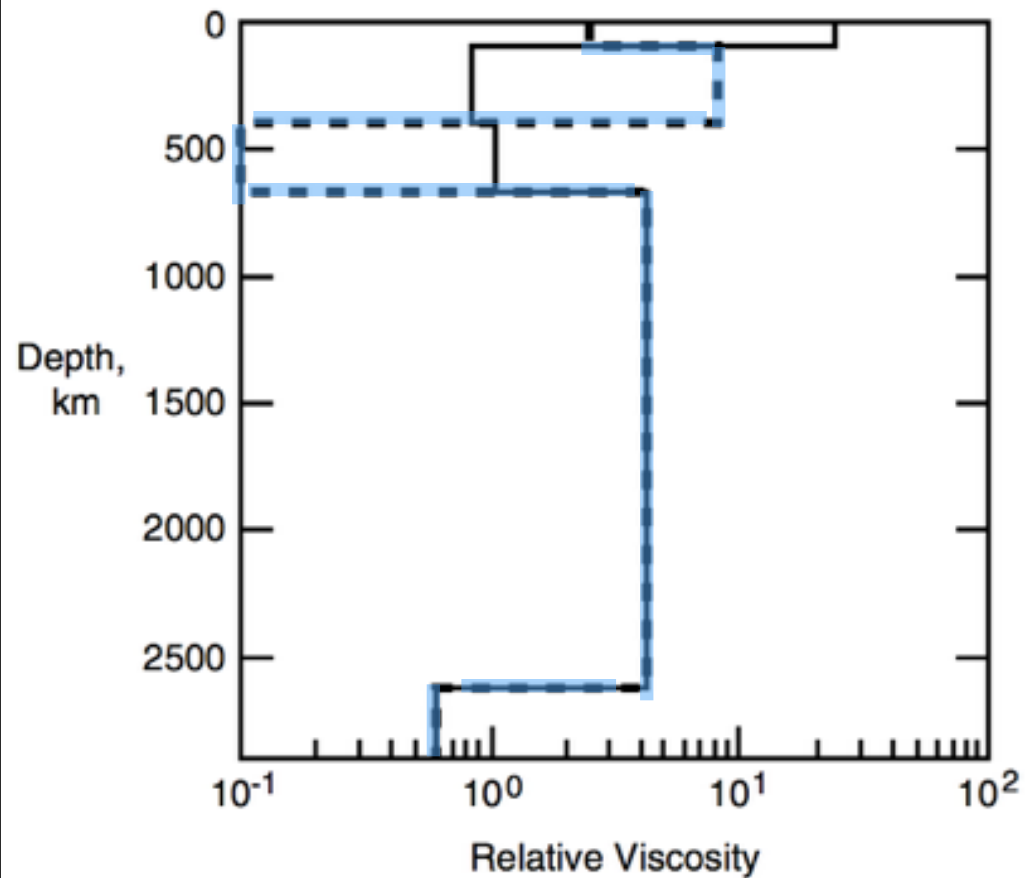


Figure 5.13. Suite of five-layer mantle viscosity profiles obtained by Forte et al. (1991) using mantle heterogeneity from seismic tomography and plate velocities. The preferred model is shown by the dashed line. The viscosity scale factor is  $10^{21}$  Pa s.

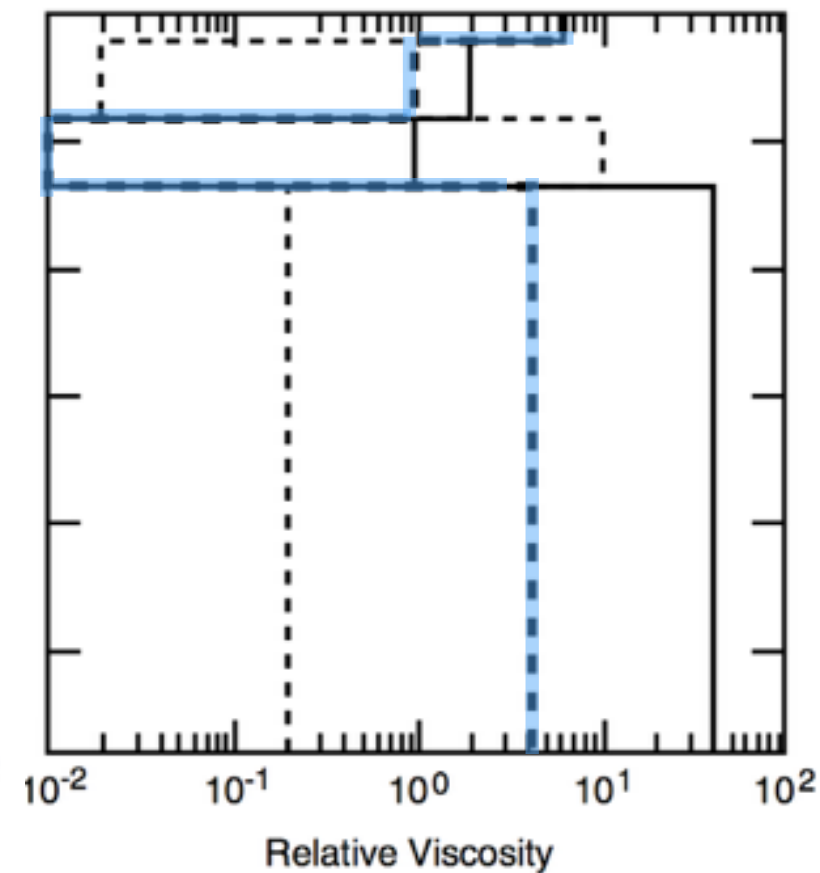


Figure 5.14. Suite of three-layer mantle viscosity profiles obtained by Ricard et al. (1989) using mantle heterogeneity from seismic tomography, plate velocities, and the geoid in a Monte Carlo inversion. The preferred model is shown by the heavy dashed line. The viscosity scale factor is  $10^{21}$  Pa s.

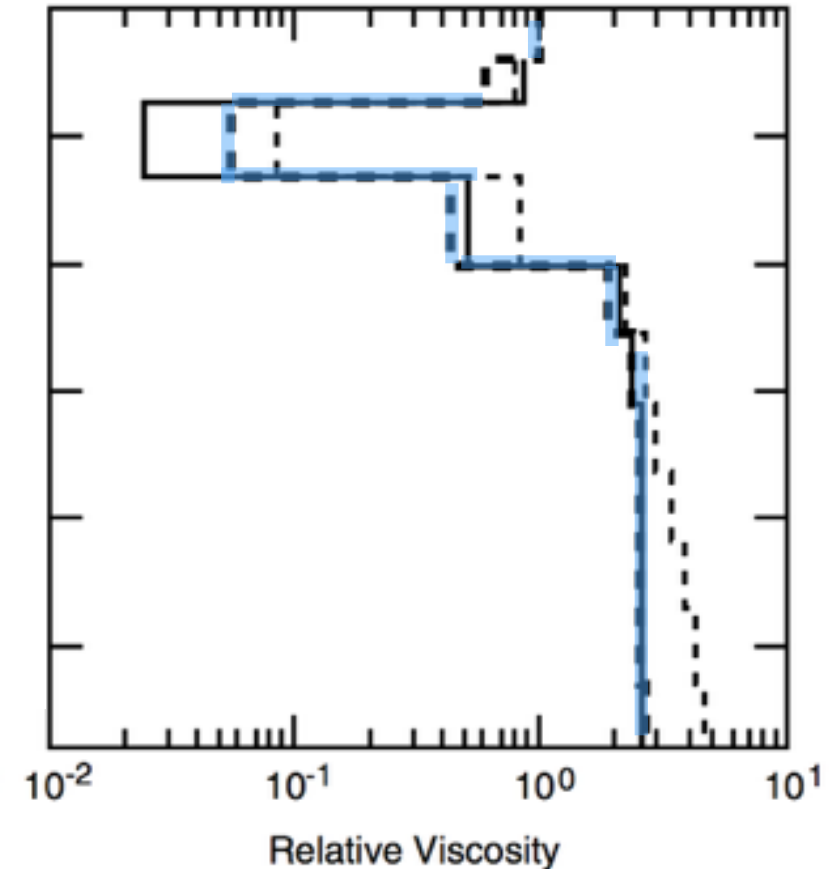
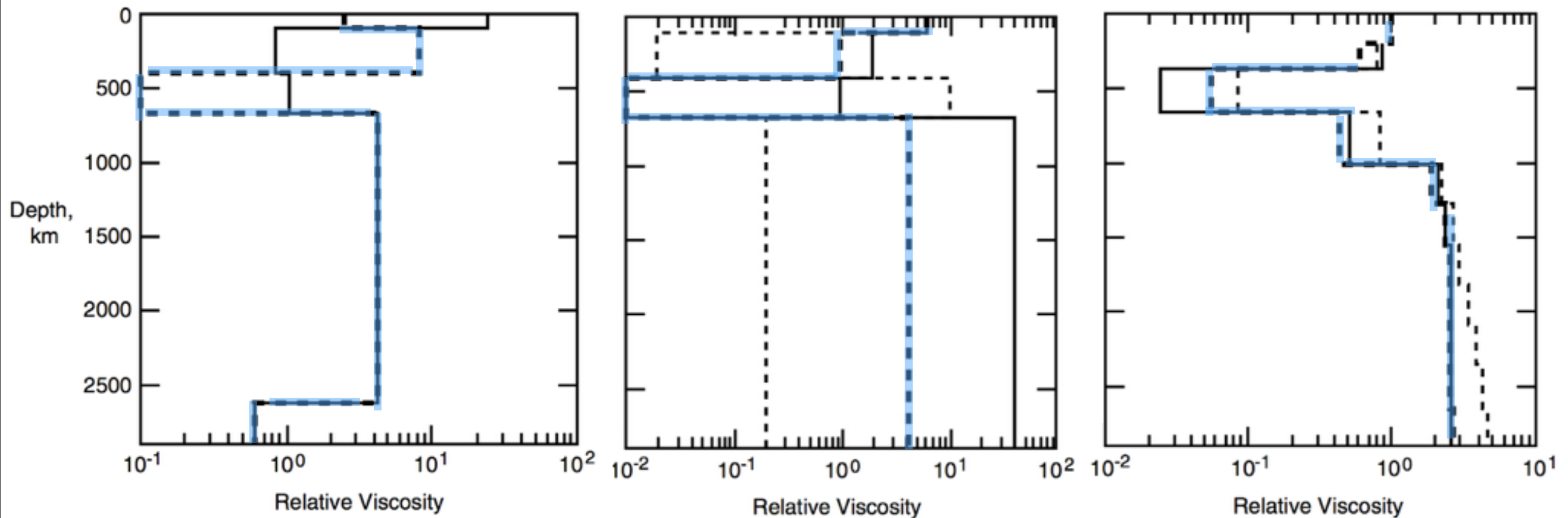


Figure 5.15. Suite of 11-layer mantle viscosity profiles obtained by King and Masters (1992) using mantle heterogeneity from S-wave tomography and the geoid. The preferred model is shown by the heavy dashed line. The viscosity scale factor is  $10^{21}$  Pa s.



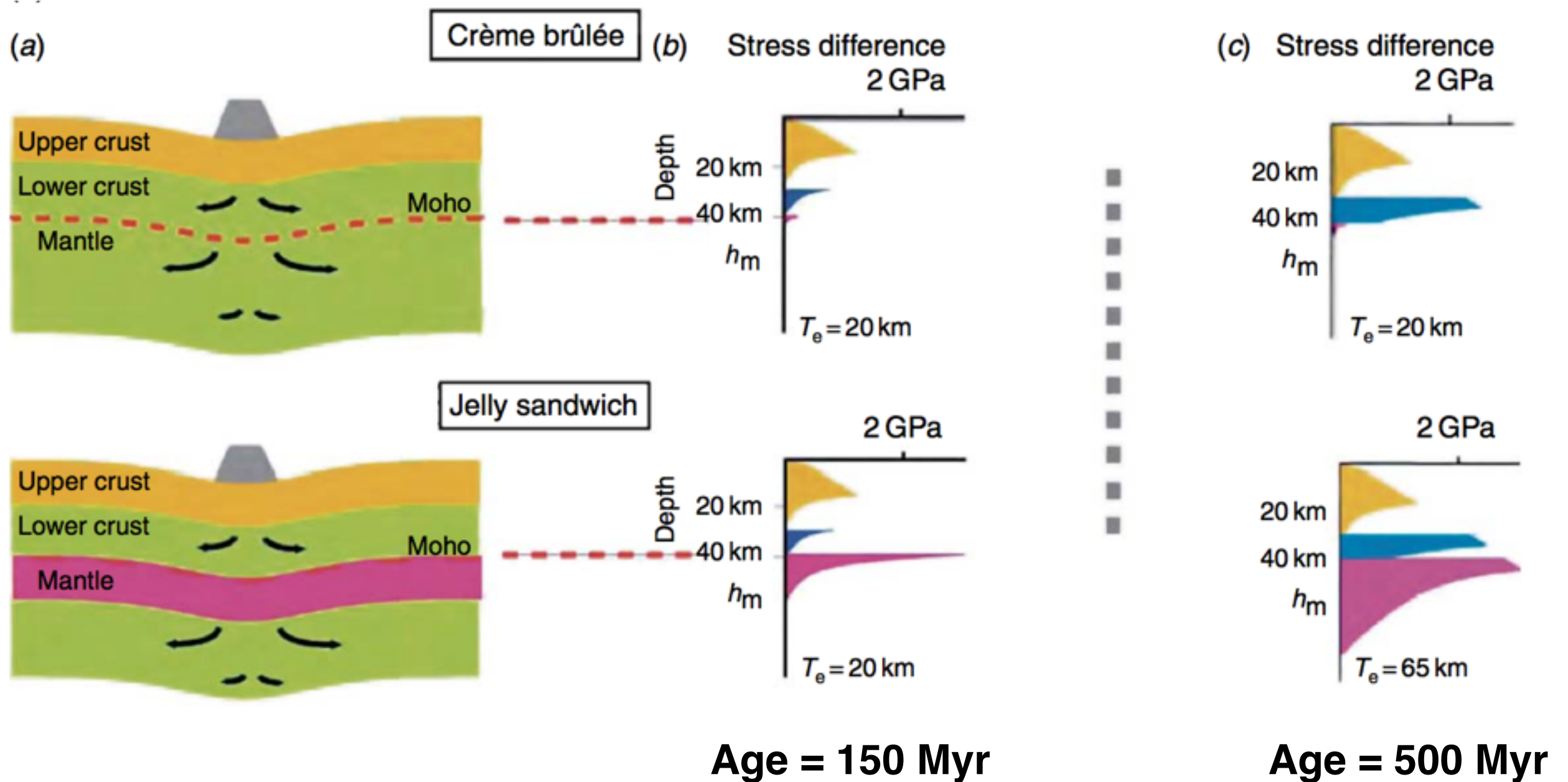
## Comparison

- Upper mantle is less viscous than the lower mantle (on average)
- Factor increase is between 3x - 30x
- Viscosity transition is at least as deep as 660 km, and may be as deep as 1200 km
- The average viscosity in the upper mantle (beneath the lithosphere) is less than  $1e21$  Pa s
- No evidence of viscosity increasing with depth, despite enormous pressure increase

# YSE validation

“Crème brûlée” versus “Jelly sandwich”  
“Jackson” versus “Classical”

*Burov & Watts (2006)*



# YSE validation

## Stability scenario

Burov & Watts (2006)

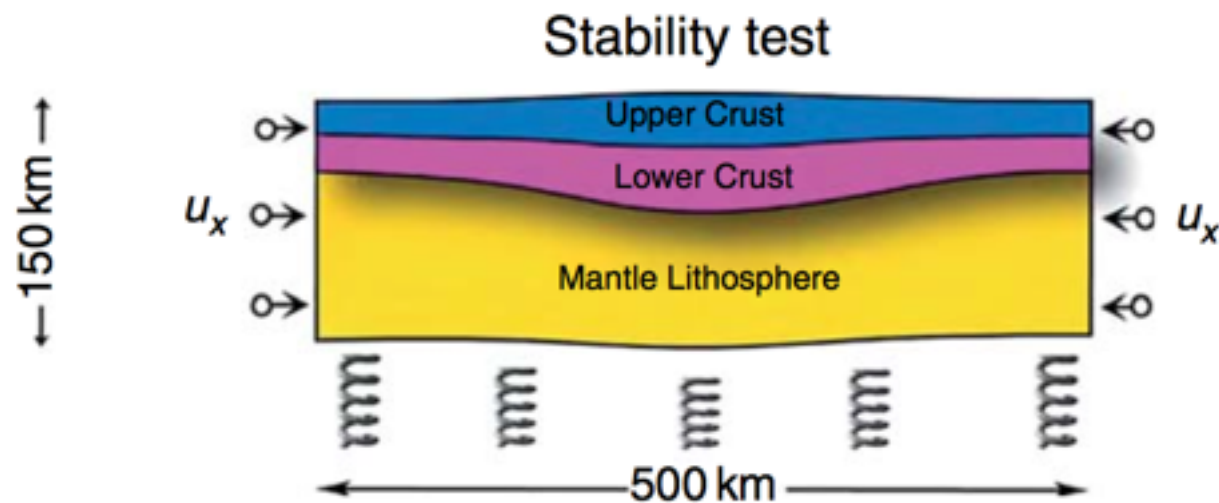
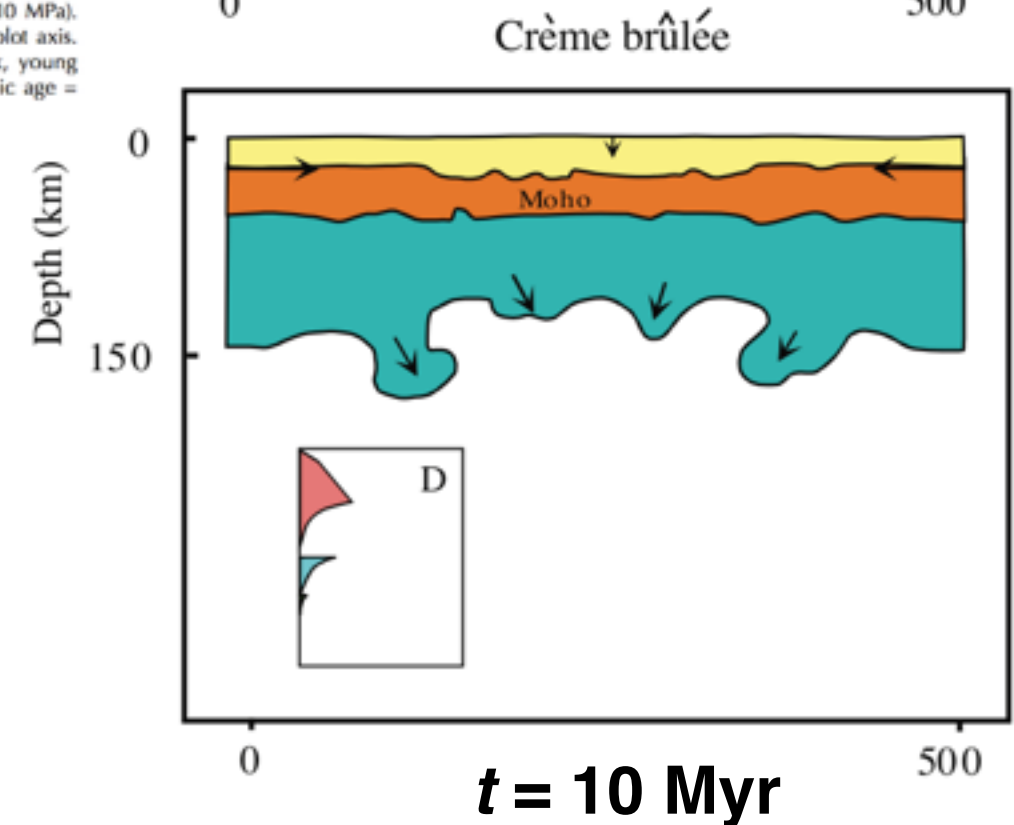
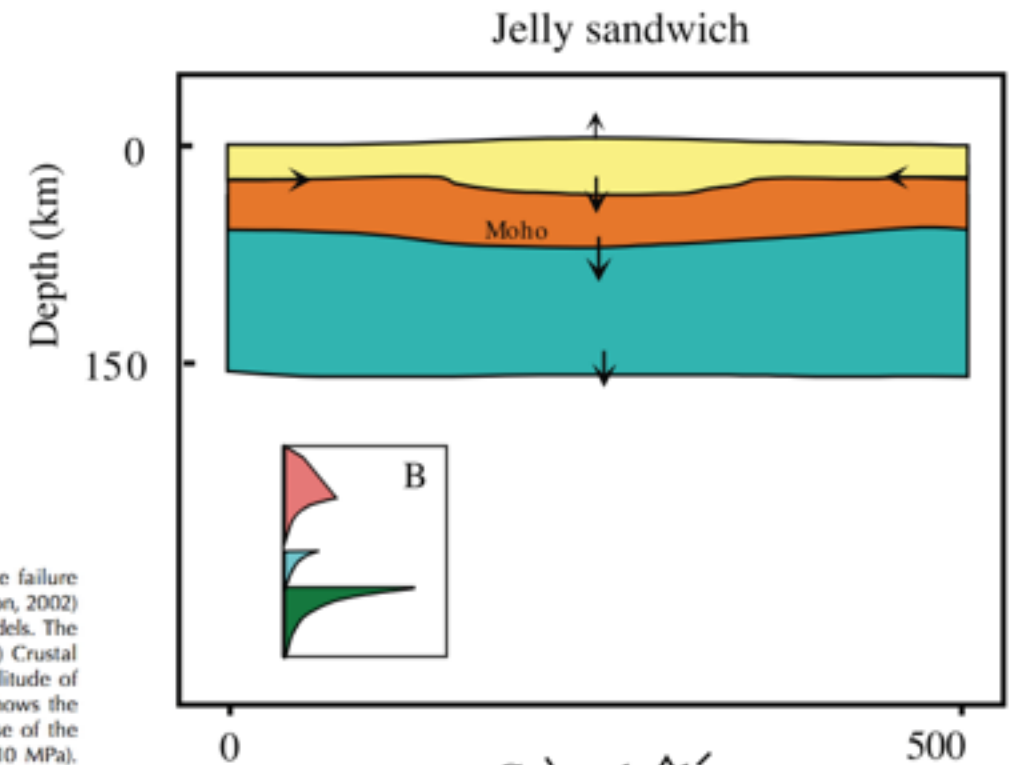


Figure 5. Tests of the stability of a mountain range using the failure envelopes associated with the jelly sandwich (Figure 5B of Jackson, 2002) and crème-brûlée (Figure 5D of Jackson, 2002) rheological models. The thermal structure is equivalent to that of a 150 Ma plate. (A) Crustal and mantle structure after 10 m.y. has elapsed. (B) The amplitude of the mantle root instability as a function of time. The figure shows the evolution of a marker that was initially positioned at the base of the mechanical lithosphere (i.e., the depth where the strength = 10 MPa). This initial position is assumed to be at 0 km on the vertical plot axis. The solid and dashed lines show the instability for a weak, young (thermotectonic age = 150 Ma) and strong, old (thermotectonic age = 500 Ma) plate, respectively.

### “CB” summary

- Instabilities develop after 1.5-2 Myr
- By 10 Myr the lithosphere starts to disintegrate. Convective removal replaces lithospheric material with hot asthenospheric material
- Flattening of the Moho, tectonic erosion of the crust root
- CB cannot explain long term persistence of topography

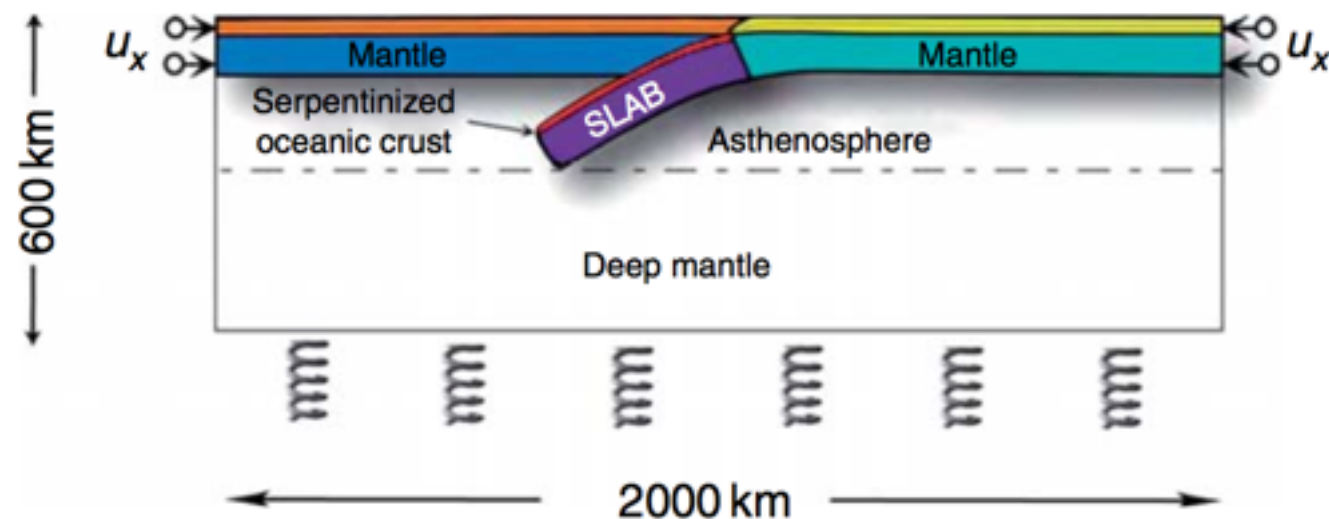


# YSE validation

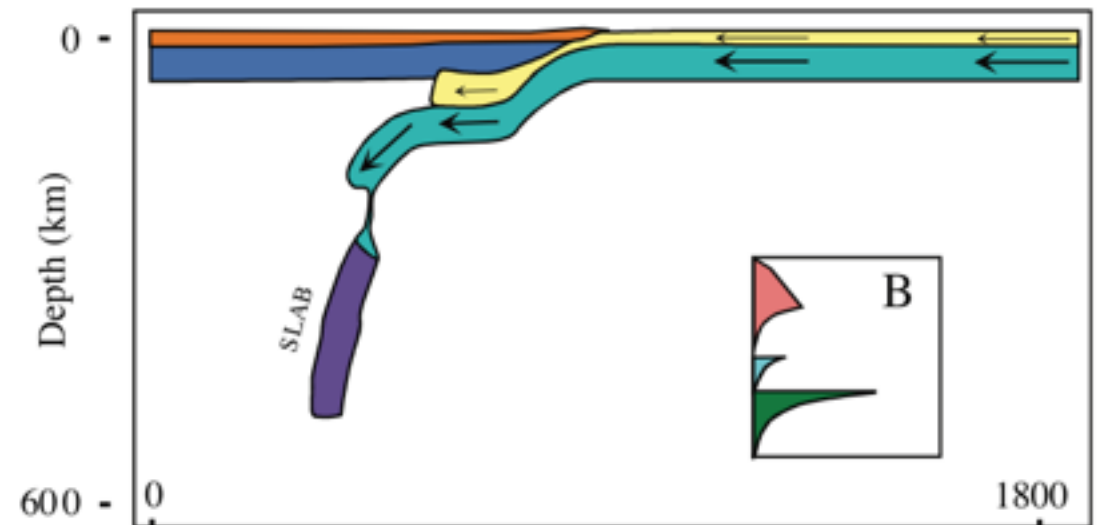
## Collision scenario

Burov & Watts (2006)

Collision test



Jelly sandwich



### “CB” summary

- CB is unstable - no subduction
- Convergence is taken up in the suture zone separation two plates
- CB cannot explain long term integrity of down going slab
- JS is consistent with structural style of collision systems associated with slab flattening, crustal doubling and arc subduction

Crème brûlée

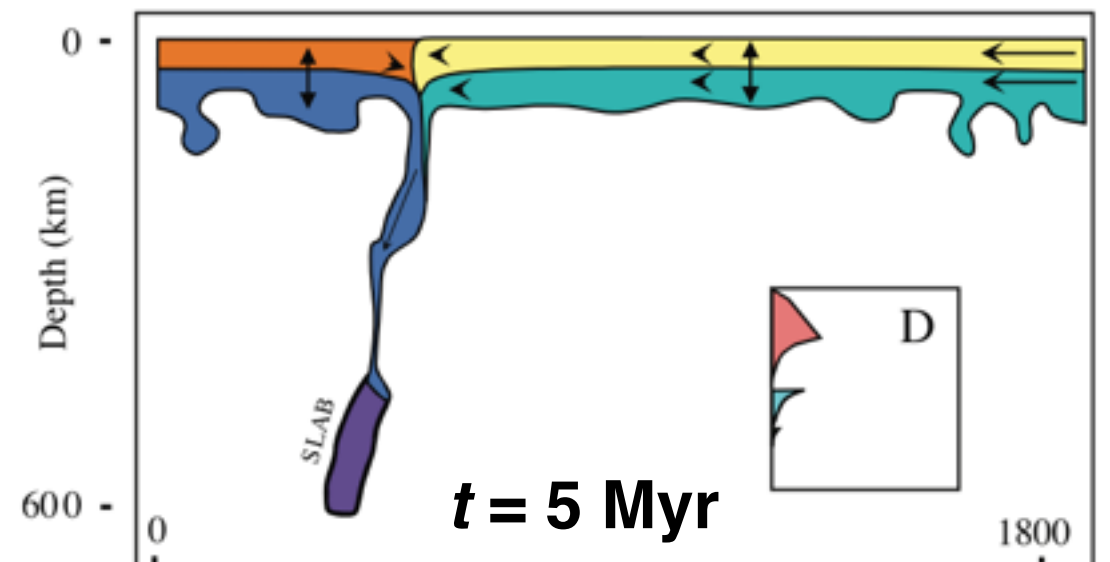


Figure 6. Tests of the stability of a continental collisional system using the failure envelopes associated with the jelly sandwich (B—Figure 5B of Jackson, 2002) and crème-brûlée (D—Figure 5D of Jackson, 2002) models. The elastic thickness,  $T_e$ , and Moho temperature are  $\sim 20$  km and  $600^\circ\text{C}$ , respectively, for both models. The figure shows a snapshot at 5 Ma of the structural styles that develop after 300 km of shortening.

# Plate motions: mantle structure

## The Dynamics of Plate Tectonics and Mantle Flow: From Local to Global Scales

Georg Stadler,<sup>1</sup> Michael Gurnis,<sup>2\*</sup> Carsten Burstedde,<sup>1</sup> Lucas C. Wilcox,<sup>1†</sup>  
Laura Alisic,<sup>2</sup> Omar Ghattas<sup>1,3,4</sup>

SCIENCE VOL 329 27 AUGUST 2010

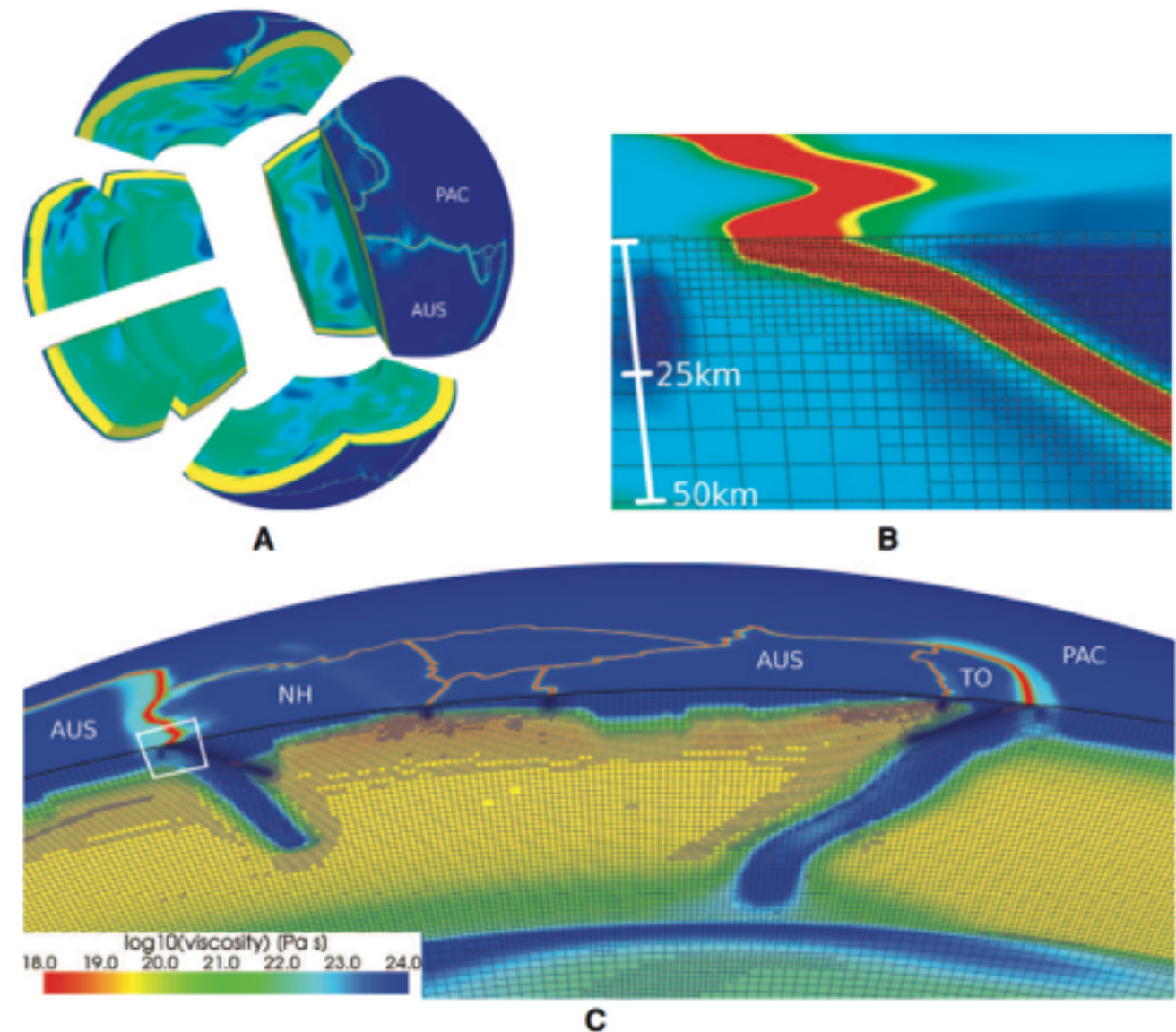
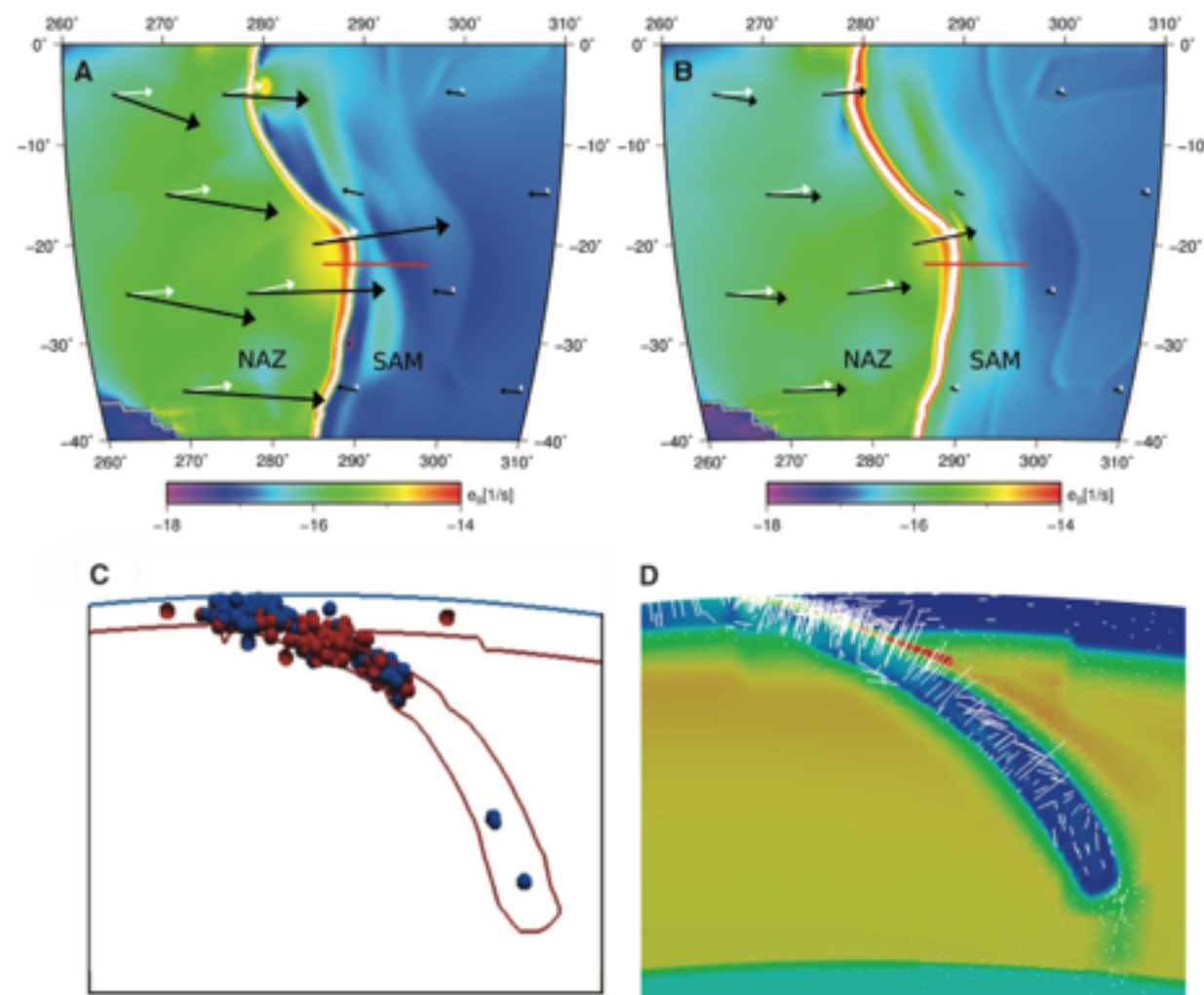


**Fig. 1.** (A) Splitting of Earth's mantle into 24 warped cubes. The effective viscosity field is shown; the narrow low-viscosity zones corresponding to plate boundaries are seen as red lines on Earth's surface. (B) Zoom into the hinge zone of the Australian plate [as indicated by the box in (C)] showing the adaptively refined mesh with a finest resolution of about 1 km. (C) Cross section showing the refinement that occurs both around plate boundaries and dynamically in response to the nonlinear viscosity, with plastic failure in the region from the New Hebrides to Tonga in the SW Pacific. Plates are labeled Australian, AUS; New Hebrides, NH; Tonga, TO; and Pacific, PAC.

# Plate motions: mantle structure

## **Multi-scale dynamics and rheology of mantle flow with plates**

Laura Alisic,<sup>1,2</sup> Michael Gurnis,<sup>1</sup> Georg Stadler,<sup>3</sup> Carsten Burstedde,<sup>3,4</sup>  
and Omar Ghattas<sup>3,5,6</sup>

Received 14 February 2012; revised 24 August 2012; accepted 31 August 2012; published 9 October 2012.

[1] Fundamental issues in our understanding of plate and mantle dynamics remain unresolved, including the rheology and state of stress of plates and slabs; the coupling between plates, slabs and mantle; and the flow around slabs. To address these questions, models of global mantle flow with plates are computed using adaptive finite elements, and compared to a variety of observational constraints. The dynamically consistent instantaneous models include a composite rheology with yielding, and incorporate details of the thermal buoyancy field. Around plate boundaries, the local resolution is 1 km, which allows us to study highly detailed features in a globally consistent framework. Models that best fit plateness criteria and plate motion data have strong slabs with high stresses. We find a strong dependence of global plate motions, trench rollback, net rotation, plateness, and strain rate on the stress exponent in the nonlinear viscosity; the yield stress is found to be important only if it is smaller than the ambient convective stress. Due to strong coupling between plates, slabs, and the surrounding mantle, the presence of lower mantle anomalies affect plate motions. The flow in and around slabs, microplate motion, and trench rollback are intimately linked to the amount of yielding in the subducting slab hinge, slab morphology, and the presence of high viscosity structures in the lower mantle beneath the slab.

**Citation:** Alisic, L., M. Gurnis, G. Stadler, C. Burstedde, and O. Ghattas (2012), Multi-scale dynamics and rheology of mantle flow with plates, *J. Geophys. Res.*, *117*, B10402, doi:10.1029/2012JB009234.

# Forward model

$$\nabla \mathbf{p} - \nabla \cdot [\eta(T, \mathbf{u})(\nabla \mathbf{u} + \nabla \mathbf{u}^T)] = \text{Ra}T \mathbf{e}_r,$$

$$\nabla \cdot \mathbf{u} = 0,$$

\* 1 km resolution at plate boundaries:  
Using adaptive finite element mesh,

—> 24 hrs on 6000 CPUs

\* Single snapshot in time

Inputs:

- rheology (flow law)
- thermal structure
- slab geometry

Outputs:

- velocity (volume/surface)
- pressure
- > plate direction, speed, “plateness”, surface strain-rate, net surface rotation
- > stress along slab, stress drop, slab strain-rate

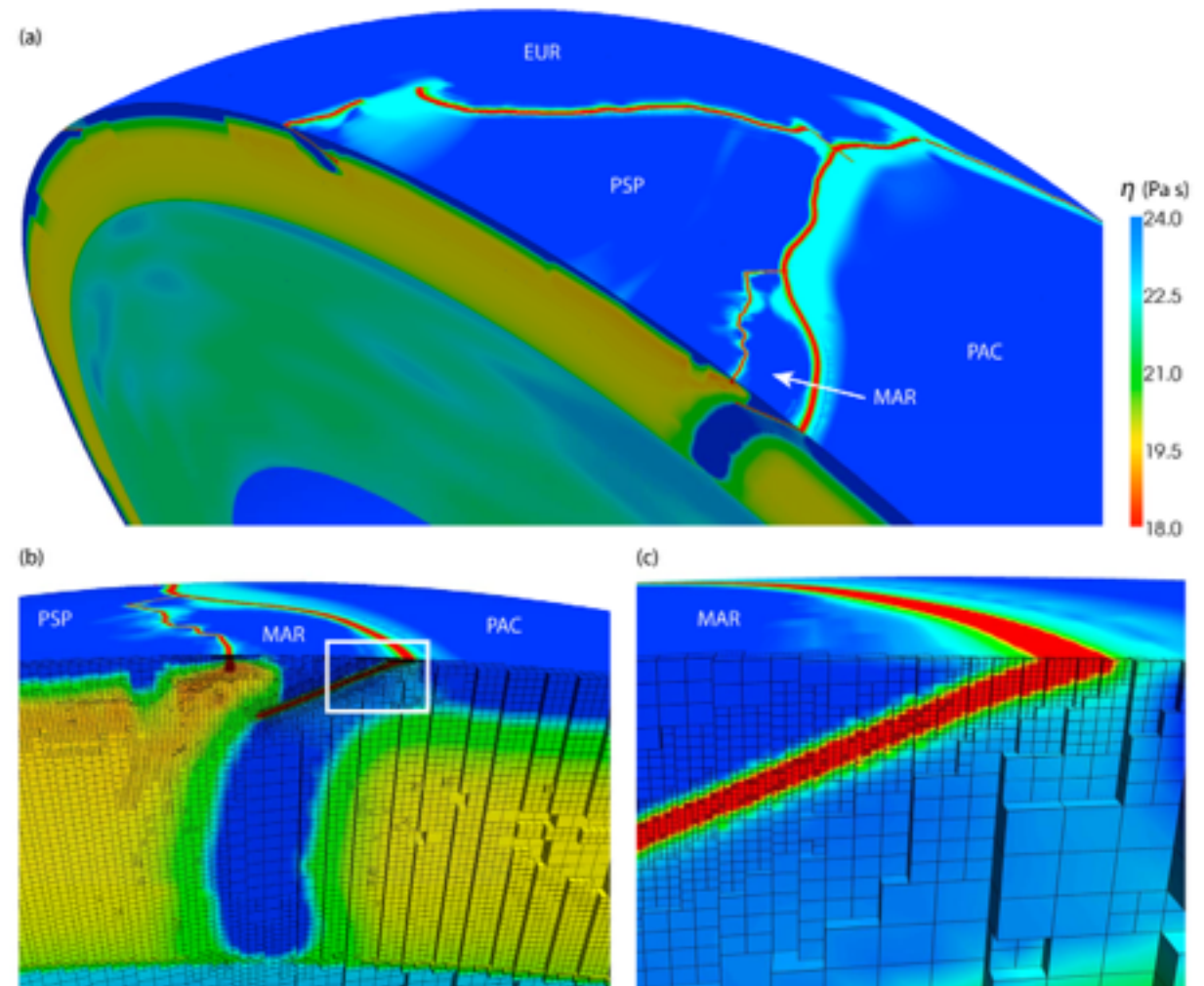


**Figure 2.** (a) Cutout showing viscosity in a global model with stress exponent  $n = 3.0$  and yield stress  $\sigma_y = 100$  MPa (Case 2) through the Marianas and Philippines. (b) Zoom-in on viscosity of the Marianas subduction zone, showing the mesh. (c) Further zoom-in on the hinge of the Marianas slab, as denoted by the white box in Figure 2b. Plate labels are: EUR: Eurasia; MAR: Marianas; PAC: Pacific; PSP: Philippine Sea.

# Thermal structure

- Convert age to temperature via half space cooling model

$$T_L(z, \tau) = T_s + (T_m - T_s) \operatorname{erf}\left(\frac{z}{2\sqrt{\kappa\tau}}\right)$$

- Age in the oceanic lithosphere (Muller et al, 2008)
- Cratons assumed to be 300 Myr old
- Regions 750 km of subduction zones, ~75 Myr
- Everywhere else, 125 Myr
- Slab age: obtained from age at the trench, just prior to subduction and propagated along the slab
- Lower mantle, S2ORTS tomography,  $\delta T = -\omega\delta V_s$
- Slab geometry (upper surface) constrained from tomography and seismicity (where available)

# Viscosity structure

- Arrhenius flow law (strain-rate and temperature dependent)
- Composite rheology utilising diffusion and dislocation creep and upper yield strength
- At convergent plate boundaries, viscosity is locally weakened along “fault surfaces” via Gaussian function

$$\eta_{df,ds} = \left( \frac{d^p}{A C_{OH}^r} \right)^{\frac{1}{n}} \dot{\epsilon}_{II}^{\frac{1-n}{n}} \exp \left( \frac{E_a + PV_a}{nRT} \right)$$

$$\eta_{comp} = \frac{\eta_{df} \eta_{ds}}{\eta_{df} + \eta_{ds}}$$

$$\sigma_y = \min \left( \sigma_o + \frac{\delta\sigma}{\delta z} z, \sigma_y^{\max} \right)$$

$$\eta_{eff} = \Gamma(\mathbf{x}) \min \left( \frac{\sigma_y}{\dot{\epsilon}_{II}}, \eta_{comp} \right)$$

$$\Gamma(\mathbf{x}) = 1 - (1 - w) \exp \left( -\frac{x_1^2}{2a^2} \right)$$

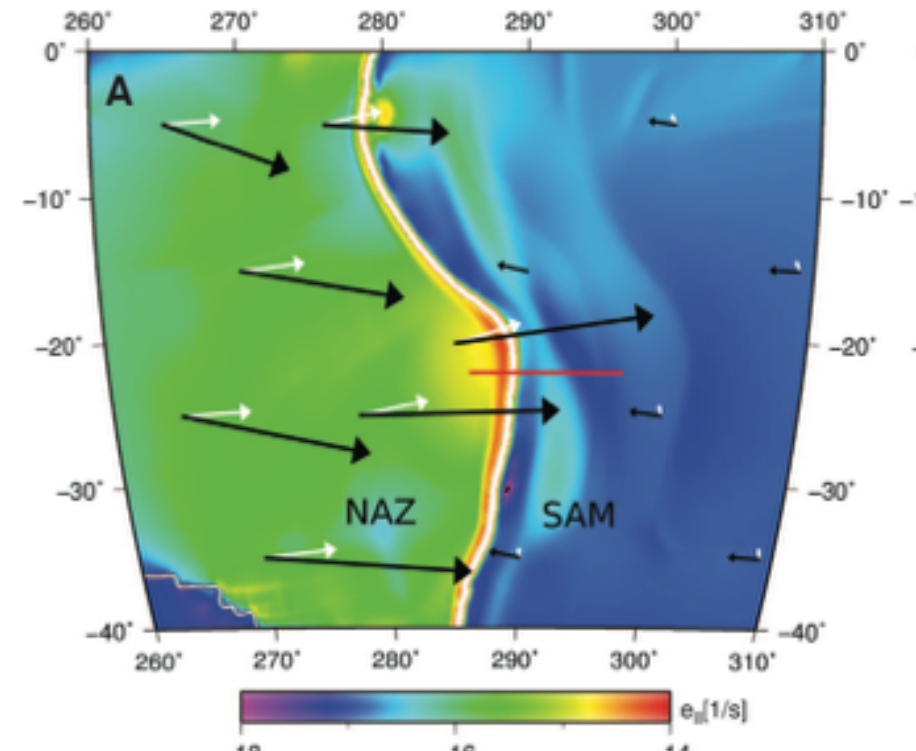
“Tuneable”  
model  
parameters

# Findings

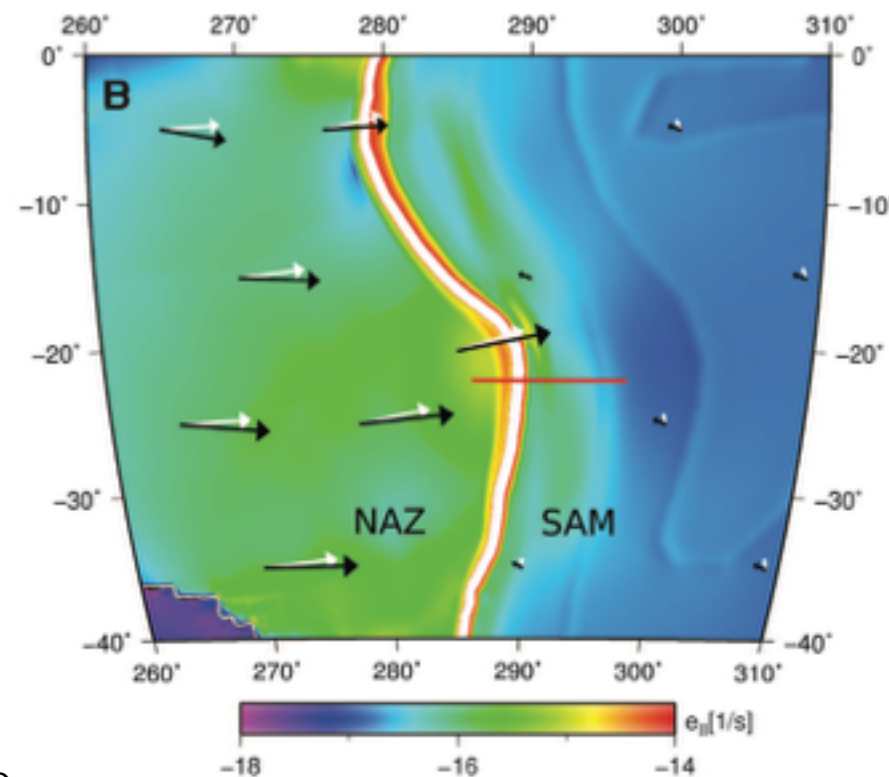
- The Pacific plate plays a dominant role in obtaining good fit to global plate motions
- Fitting plate motions accurately required:
  - a yield stress of 100 MPa, despite laboratory data suggesting it should be ~500-1000 MPa
  - a power-law exponent of  $n = 3$
- An exponent of  $n = 3.5$  results high plate velocities and surface rotations
- The viscosity in slab hinges is  $\sim 1e22$  Pa s
- Slabs are strong and have a viscosity  $\sim 1e24$  Pa s
- Major plates more affected by changes in yield stress than micro-plates (opposite behaviour when increasing power-law exponent due to decoupling)
- Lateral flow around slabs is trench perpendicular
- Changes in density structure in lower mantle affect plate motions  $\rightarrow$  strong coupling between plates, slabs and upper/lower mantle
- Plates penetrating the lower mantle move slowly c.f. those that do not

# Findings

- Best fit models have
  - viscosity in slab hinges is  $\sim 1e22$  Pa s
  - strong slabs with a viscosity  $\sim 1e24$  Pa s
- An exponent of  $n = 3.5$  results high plate velocities and surface rotations
- Higher exponents result in weaker slabs - reducing decoupling with the lower mantle



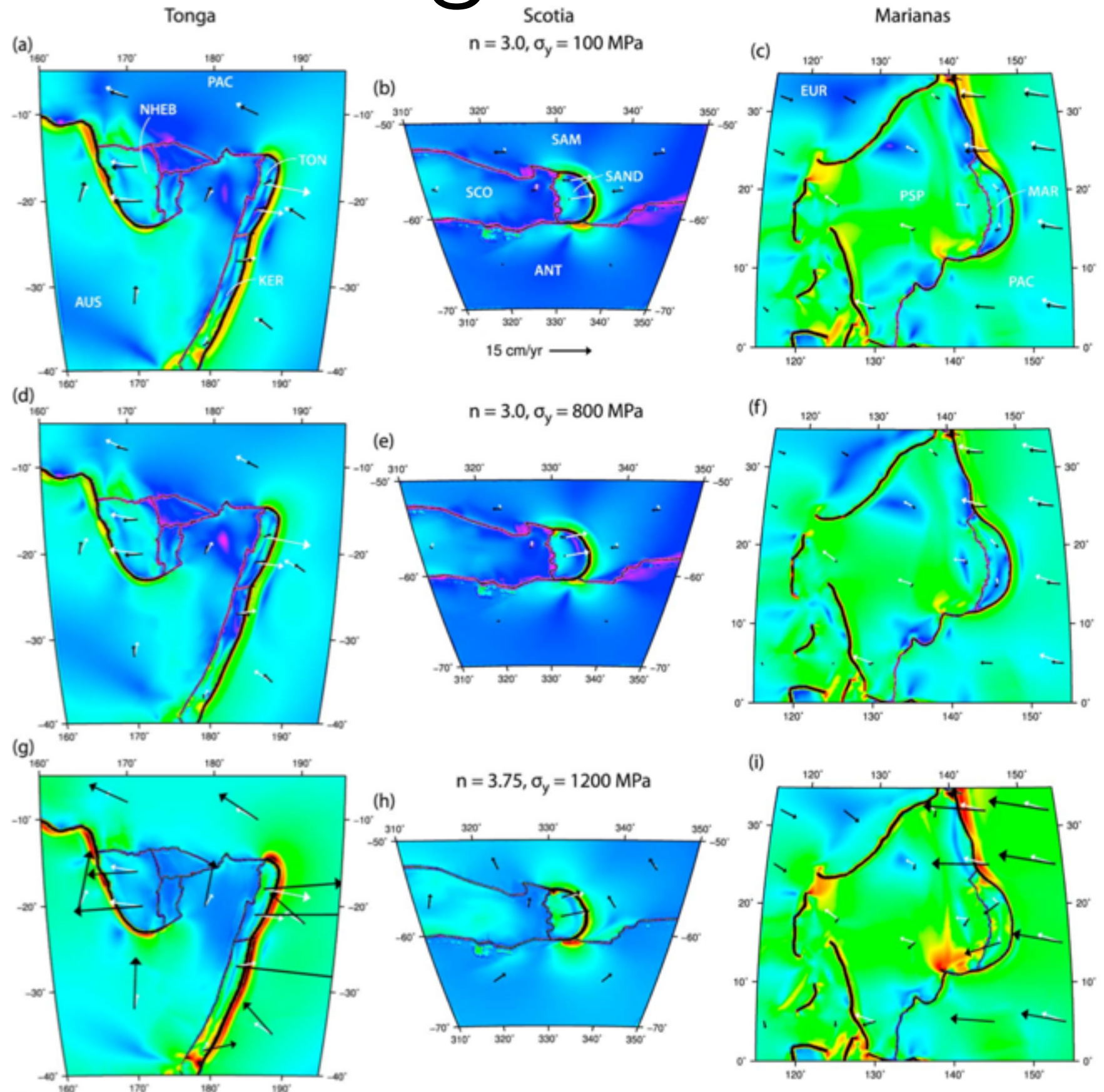
$n = 3.5$   
(weak)



$n = 3$   
(strong)

# Findings

- An exponent of  $n = 3.5$  results high plate velocities and surface rotations
- Major plates more affected by changes in yield stress than micro-plates (opposite behaviour when increasing power-law exponent due to decoupling)



# Summary

- Viscosity constraints can be obtained via a wide varied of different techniques:
  - laboratory; geology / geophysics; numerics
- All methods possess different trade-offs / weakness
- A robust characteristic amongst all methods is that the viscosity of the lower mantle is higher than that of the upper mantle. Lower mantle viscosity estimates are on the order of  $1e21$  Pa s and  $1e22$  Pa s
- YSEs should not be taken literally (strain-rates are depth dependent)
- *A complete picture of the radial and lateral viscosity structure, both globally and regionally, within the crust and lithosphere is an on-going and active area of geodynamic research*